



Direct numerical simulation of turbulent heat transfer on the Reynolds analogy over irregular rough surfaces

メタデータ	言語: eng 出版者: 公開日: 2022-04-19 キーワード (Ja): キーワード (En): 作成者: Kuwata, Yusuke メールアドレス: 所属:
URL	http://hdl.handle.net/10466/00017659

Direct numerical simulation of turbulent heat transfer over irregular rough surfaces based on Reynolds analogy

Y. Kuwata*

*Department of Mechanical Engineering, Osaka Prefecture University, Sakai, Osaka
599-8531, Japan*

Abstract

The effect of rough surface topography on heat and momentum transfer is studied by direct numerical simulations of turbulent heat transfer over uniformly heated three-dimensional irregular rough surfaces, where the effective slope and skewness values are systematically varied while maintaining a fixed root-mean-square roughness. The friction Reynolds number is fixed at 450, and the temperature is treated as a passive scalar with a Prandtl number of unity. Both the skin friction coefficient and Stanton number are enhanced by the wall roughness. However, the Reynolds analogy factor for the rough surface is lower than that for the smooth surface. The semi-analytical expression for the Reynolds analogy factor suggests that the Reynolds analogy factor is related to the skin friction coefficient and the difference between the temperature and velocity roughness functions, and the Reynolds analogy factor for the present rough surfaces is found to be predicted solely based on the equivalent sand-grain roughness. This suggests that the relationship between the Reynolds analogy factor and the equivalent sand-grain roughness

*corresponding author

Email address: kuwata@me.osakafu-u.ac.jp (Y. Kuwata)

is not affected by the effective slope and skewness values. Analysis of the heat and momentum transfer mechanisms based on the spatial- and time-averaged equations suggests that two factors influence the Reynolds analogy factor. One is the increased effective Prandtl number within the rough surface in which the momentum diffusivity due to the combined effects of turbulence and dispersion is larger than the corresponding thermal diffusivity. The other is the significant increase in the pressure drag force term above the mean roughness height.

Keywords: Direct numerical simulation, Rough wall, Turbulent heat transfer, Lattice Boltzmann method,

Nomenclature

A : plane area of an $x - z$ plane: $A = L_x L_z$

A_f : fluid phase plane area of an $x - z$ plane

A_r : surface area of a rough surface

B : log-law intercept of the mean velocity profile for smooth wall turbulence

c : specific heat

C : model constant

C_f : skin friction coefficient at a rough wall: $C_f = \frac{\tau_w^a}{0.5\rho U_b^2}$

C_{f0} : skin friction coefficient at a smooth wall

ES : effective slope of a rough surface

f_k : model function for the correlation of S_t

f_{p_i} : mean pressure drag in an $x - z$ plane

f_{v_i} : mean viscous drag in an $x - z$ plane

Fp_i : contribution of pressure drag to the total shear stress

Fv_i : contribution of viscous drag to the total shear stress

h : surface height of a rough surface

h_m : mean surface height

h_p : peak height of a rough surface

h_{pe} : peak height of a rough surface measured by y_e

h_{rms} : root mean square of the surface height elevation

h_t : mean peak-to-valley height

H_i : plane-averaged turbulent heat flux

\mathcal{H}_i : plane-dispersion heat flux

H_w : wall heat flux contribution to the total heat flux

I^+ : gap between the temperature and velocity profiles: $I^+ = \langle \bar{\theta} \rangle^+ - \langle \bar{u} \rangle^+$

I_{td}^+ : contribution of turbulence and dispersion transport to I^+

I_{tot}^+ : contribution of total heat flux and shear stress to I^+

I_{wi}^+ : contribution of wall interaction term to I^+

k_s : equivalent sand-grain roughness

Ku : kurtosis factor of a surface elevation

ℓ_y : length scale related to a surface area gradient in terms of y : $\ell_y = \frac{\partial A_r}{\partial y}$

ℓ_x : length scale related to a surface area gradient in terms of x : $\ell_x = \frac{\partial A_r}{\partial x}$

L : obstacle perimeter within an $x - z$ plane

L_x : computational domain length in the x -direction

L_y : computational domain length in the y -direction

L_z : computational domain length in the z -direction

n_i : unit normal vector pointing outward from the fluid to solid phase

p : pressure

Pr : molecular Prandtl number

Pr_t : turbulent Prandtl number

Pr_{eff} : effective Prandtl number: $Pr_{eff} = \frac{\nu_{eff}}{\alpha_{eff}}$

q_w : wall heat flux

q_w^a : equivalent wall heat flux: $q_w^a = q_w \frac{A_r}{A}$

Q : flow rate

R_{ij} : $x - z$ plane-averaged Reynolds stress: $R_{ij} = \langle \overline{u'_i u'_j} \rangle$

RA : Reynolds analogy factor for a rough wall: $RA = \frac{2S_t}{C_f}$

RA_0 : Reynolds analogy factor for a smooth wall: $RA_0 = \frac{2S_{t0}}{C_{f0}}$

Re_τ : friction Reynolds number: $Re_\tau = \frac{u_\tau \delta_e}{\nu}$

s_{cht} : source term for the constant heat flux condition

s_t : tortuosity molecular diffusion term

s_w : wall heat transfer term

Sk : skewness factor of surface elevation

S_t : Stanton number at a rough wall

S_{t0} : Stanton number at a smooth wall

t : time

t_τ : friction temperature: $t_\tau = \frac{q_w^a}{\rho c u_\tau}$

T : temperature

T_w : temperature at a rough surface

\mathcal{T}_{ij} : $x - z$ plane-dispersion stress: $\mathcal{T}_{ij} = \langle \tilde{u}_i \tilde{u}_j \rangle$

u_i : velocity

u_τ : friction velocity: $u_\tau = \sqrt{\frac{\tau_w^a}{\rho}}$

U_b : bulk mean velocity: $U_b = \frac{Q}{\delta_e L_z}$

x : streamwise coordinate

y : wall normal coordinate

y' : normal distance from a mean surface height: $y' = \frac{y-h_m}{h_m}$

y_e : effective wall normal distance: $y_e = \int_0^y \varphi dy$

z : spanwise coordinate

α : thermal diffusivity

α_{eff} : effective thermal diffusivity

β : log-law intercept of the mean temperature profile for smooth wall turbulence

δ : half channel height

δ_e : effective half channel height: $\delta_e = \delta - h_m$

Δ : grid spacing

ΔP : mean pressure difference between the inlet and outlet boundary faces

ΔU^+ : velocity roughness function

ΔU_{ir}^+ : contribution of the viscous term related to the roughness density variation to ΔU^+

ΔU_{pd}^+ : contribution of the pressure drag to ΔU^+

ΔU_{td}^+ : contribution of the Reynolds and dispersion stresses to ΔU^+

ΔU_{vd}^+ : contribution of the viscous drag to ΔU^+

$\Delta \Theta^+$: temperature roughness function

$\Delta\Theta_{ir}^+$: contribution of the conduction term related to the roughness density variation to $\Delta\Theta^+$

$\Delta\Theta_{td}^+$: contribution of the turbulent and dispersion heat fluxes to $\Delta\Theta^+$

$\Delta\Theta_{tot}^+$: contribution of the total heat flux to $\Delta\Theta^+$

$\Delta\Theta_{fig12}^+$: contribution of the wall heat transfer to $\Delta\Theta^+$

κ : Kármán constant

θ : temperature variance: $\theta = T_w - T$

Θ_a : arithmetic mean temperature of θ

Θ_m : bulk mean temperature of θ

ν : kinematic viscosity

ν_{eff} : effective viscosity

ρ : fluid density

τ_w^a : wall shear stress at a rough surface

φ : $x - z$ plane porosity: $\varphi = \frac{A_f}{A}$

ϕ : variable

ϕ' : fluctuation of ϕ : $\phi - \bar{\phi}$

$\bar{\phi}$: time-averaged value of ϕ

$\langle\phi\rangle$: superficial $x - z$ plane-averaged value of ϕ

$\langle \phi \rangle^f$: intrinsic $x - z$ plane-averaged value of ϕ

$\tilde{\phi}$: plane-dispersion of ϕ : $\phi - \langle \phi \rangle^f$

$()^+$: value normalized by the inner-scaled (u_τ, t_τ , and ν)

1. Introduction

The transport of momentum, mass, and heat for rough wall turbulence has received considerable attention because the presence of wall roughness generally leads to an enhancement of those transports, resulting in a considerable increase in the skin friction coefficient, heat, and mass transfer rate. Practical examples of wall roughness include biofouling on a ship hull (Townsin et al., 1981; Schultz, 2007); deposition and pitting on internal combustion engines (Zerda et al., 1999; Forooghi et al., 2018b); turbomachinery (Acharya et al., 1986; Bons et al., 2001; Bons, 2002); and aircraft icing (Bragg et al., 1986; Lynch and Khodadoust, 2001). In all these cases, the machine performance was significantly degraded by the roughness. Meanwhile, as the wall roughness enhances the heat transfer performance, artificial roughness is frequently created in engineering devices, such as internal cooling inside turbine blades (Mochizuki et al., 1999; Murata and Mochizuki, 2001), solar thermal systems (Chamoli et al., 2012), and heat transfer pipes (Gee and Webb, 1980; Akermann et al., 2020). Therefore, considerable effort has been made in understanding and predicting the effects of wall roughness on momentum and scalar transport.

An earlier study on the effects of wall roughness on momentum transfer was conducted by Nikuradse (1933), who measured the pressure drop in

pipes with walls covered by sand-grains. He found that, at a sufficiently high Reynolds number flow, the skin friction coefficient at a rough surface depends only on the relative sand-grain size. Subsequently, the so-called roughness function ΔU^+ was introduced by Clauser (1954); Hama (1954) to quantify the increase in the skin friction coefficient in a range of flow configurations, such as pipes, ducts, channels, and boundary layers. The roughness function is defined as a downward shift in the inner-scaled streamwise mean velocity relative to the smooth wall at the corresponding friction Reynolds number. It is expressed as a function of the equivalent sand-grain roughness k_s , which is the size of the sand-grain in Nikuradse (1933) that yields the same skin friction coefficient as the surface of interest. Since their earlier works, most studies have focused on how to relate the topological parameters of the rough surface to k_s or ΔU^+ , with the aim of predicting the effects of wall roughness on momentum transfer.

Earlier studies on k_s were based on the solidity parameter (Schlichting, 1937; Dvorak, 1969; Dirling, 1973; Sigal and Danberg, 1990; Van Rij et al., 2002). The pioneering work on the effects of solidity on k_s was conducted by (Schlichting, 1937) who investigated the surfaces roughened by spherical, cone, and plate roughness with varying solidity. Dirling (1973) first presented a correlation for k_s of arbitrary rough surfaces by using the ratio of the average element space to the roughness height as the solidity parameter. A subsequent study by Sigal and Danberg (1990); Van Rij et al. (2002) extended this idea to various types of rough surfaces by employing the ratio of the surface area before adding roughness to the total frontal area. Another representation of solidity, which is significantly easier to define for

three-dimensional irregular roughness, is the effective slope (ES) proposed by Napoli et al. (2008). The effective slope is defined as the mean slope of the undulation and corresponds to double the solidity parameter, as defined by Sigal and Danberg (1990); Van Rij et al. (2002). Several numerical and experimental studies have established that ΔU^+ increases with ES when the ES value is lower than a certain threshold value, whereas ΔU^+ is independent of ES above the threshold value (Napoli et al., 2008; Schultz and Flack, 2009; De Marchis, 2016; MacDonald et al., 2016; Kuwata and Nagura, 2020).

The other important characteristic parameter that has a significant impact on k_s is the skewness factor Sk . The skewness factor is related to the statistical moments of the surface elevation, and quantifies the asymmetry of the probability density function (PDF) of the surface height elevation. An earlier attempt to relate the statistical moments to k_s was made by Musker (1980). Moreover, the importance of Sk in predicting k_s has been established using a large amount of experimental data (Flack and Schultz, 2010; Flack et al., 2016) and direct numerical simulation (DNS) data (Forooghi et al., 2017; Thakkar et al., 2017; Kuwata and Kawaguchi, 2019; Kuwata and Nagura, 2020).

With regard to the turbulent heat transfer over a rough surface, the modification of heat transfer due to the wall roughness has also been investigated extensively. The experimental studies by Nunner (1956); Dipprey and Sabersky (1963); Gowen and Smith (1968); Yaglom and Kader (1974); Kays and Crawford (1993) examined a predictive correlation for the Stanton number, S_t , at the rough surface. The pioneering experiments by Nunner (1956) on a surface roughened by two-dimensional transverse ribs offered an empirical

expression for S_t with the Reynolds number, Prandtl number, and the ratio of the rough to smooth skin friction coefficients. A semi-analytical expression for S_t based on the law of the wall similarity was proposed by Dipprey and Sabersky (1963), who demonstrated that S_t was expressed as a function of the Prandtl number, skin friction coefficient, and inner-scaled equivalent sand-grain roughness. In this expression, the effects of k_s on S_t , which cannot be analytically derived, were expressed based on the experimental data from a pipe with sand-grain roughness. The validity of this expression has been widely studied experimentally and numerically, and a modified expression has been proposed (Webb et al., 1971; Kays and Crawford, 1993; Wassel and Mills, 1979; Bons, 2002). Most of the experimental studies reached a consensus that the increase in the skin friction coefficient was greater than the associated increase in heat transfer. That is, the wall roughness weakens the similarity between the momentum and heat transfers, which was also supported by the theoretical study by Katoh et al. (2000). However, there is still much controversy about the effects of k_s on S_t . Furthermore, owing to experimental difficulties in obtaining high-fidelity temperature fields within the roughness sublayer, the underlying physics of the effects of wall roughness on heat transfer is still unclear.

Meanwhile, recent developments in computer technology have enabled us to perform DNSs for turbulent heat transfer over resolved rough surfaces (Miyake et al., 2001; Nagano et al., 2004; Forooghi et al., 2018b,a; Peeters and Sandham, 2019; MacDonald et al., 2019). The minimal-span channel DNSs on turbulent heat transfer over a surface with sinusoidal roughness performed by MacDonald et al. (2019) suggested that the correlation func-

tion proposed by Dipprey and Sabersky (1963) provided a faithful account of the effects of the equivalent sand-grain roughness on S_t . An analysis of instantaneous temperature fields suggested that the dissimilarity between the heat and momentum transfer was due to the pressure drag acting on the rough wall, which enhanced the momentum transfer but not the heat transfer. Peeters and Sandham (2019) conducted DNSs for grit-blasted surfaces and reported the considerable potential of the correlation proposed by Dipprey and Sabersky (1963) for predicting S_t for grit-blasted surfaces. The dissimilarity between the heat and momentum transfers was distinct in the recirculation zone behind the roughness elements, where the effective Prandtl numbers rapidly increased within the rough surface.

The aforementioned DNS studies concluded that the presence of pressure is closely related to the dissimilarity between heat and momentum transfer. However, it is still unclear how pressure leads to the breakdown of the Reynolds analogy. Moreover, despite the potential of modern supercomputers to perform DNSs, only a few simulations have been conducted on turbulent heat transfer over three-dimensional irregular rough surfaces. The present study has two main objectives. One is to understand the isolated effects of the effective slope and skewness factor on the heat transfer over an irregular rough surface, both of which have a considerable effect on the momentum transfer. The other is to quantify the effects of pressure on the dissimilarity between heat and momentum transfer and understand the underlying physics on the dissimilarity between them.

2. Methodology

2.1. Flow geometry

As in the previous DNS studies (Coceal et al., 2006; Leonardi and Castro, 2010; Forooghi et al., 2017; Kuwata and Kawaguchi, 2018, 2019; Kuwata and Nagura, 2020), we chose a rough-walled open-channel flow configuration as shown in Figure 1 to simulate the turbulence modification near a rough surface with fewer computational resources. Three-dimensional irregular rough walls were considered for the bottom wall, whereas a symmetric boundary condition was considered for the top boundary. The computational domain size (L_x, L_y, L_z) is $(6\delta, \delta, 3\delta)$, in the streamwise, wall-normal, and spanwise directions, respectively, where δ is the half-channel height. The domain size is identical to those used in the rough-walled open-channel flow DNS studies conducted by Kuwata and Kawaguchi (2018, 2019); Kuwata et al. (2020), and was confirmed to be sufficient through a preliminary simulation with a computational domain that was twice as large. The flow was periodic in the streamwise and spanwise directions. The flow was driven by a constant streamwise pressure difference, and the friction Reynolds number based on the effective half-channel height $\delta_e = \delta - h_m$ with h_m being the mean rough surface height, was fixed at $Re_\tau = 450$.

For the thermal boundary conditions, the adiabatic boundary condition was applied to the top boundary, whereas the modified mixed boundary conditions were applied for the rough surface, in which a statistically uniform heat flux in space and time is prescribed. This boundary condition was originally proposed by Kasagi et al. (1992) for the smooth wall turbulence, and has been widely used in DNS studies (Kawamura et al., 1998; Abe et al.,

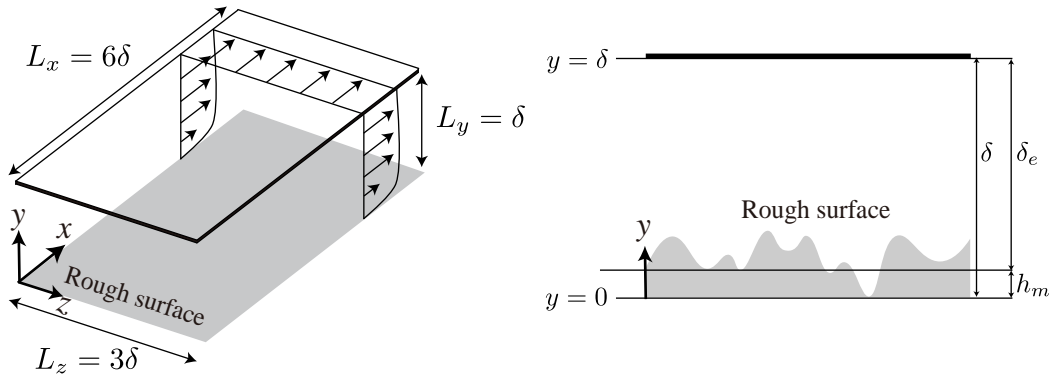


Figure 1: Sketch of the computational geometry of a rough-walled open-channel flow.

2004; Kozuka et al., 2009; Lluesma-Rodríguez et al., 2018). The extension of this approach for the rough surface is available in Appendix A. The fluid Prandtl number was set to unity, $Pr = 1.0$, and we assumed a passive scalar by neglecting the buoyancy effect.

2.2. Numerical method

We employed the lattice Boltzmann method (LBM) as the numerical method in this study. The LBM solves the time evolution of the particle distribution function based on the discretized gas kinetic equations, and is proven to recover the continuity and Navier–Stokes equations in second-order accuracy in space and time. Although there are several possible choices for the LBM models, we used the three-dimensional 27 discrete velocity (D3Q27) multiple-relaxation-time LBM (Suga et al., 2015) for the flow field, whereas the scalar field was simulated using the three-dimensional 19 discrete velocity (D3Q19) regularized LBM (Latt and Chopard, 2006; Suga et al., 2017). Note that the LBM approach has been extensively validated against fundamental flows (Suga et al., 2015) and applied to simulate the turbulent heat trans-

fer of complicated flow geometries (Suga et al., 2017; Nishiyama et al., 2020; Kuwata and Nagura, 2020). A regular grid with an equal spacing of $\Delta^+ \simeq 1.8$ was used, where Δ^+ is the grid spacing in wall unit defined as $\Delta u_\tau/\nu$, where ν and u_τ denote the kinematic viscosity and friction velocity, respectively. The number of grid points was $1680(x) \times 281(y) \times 840(z)$, resulting in a total of 397 million grid points. This spatial resolution was confirmed to be sufficient to accurately resolve fine-scale turbulence near the rough surface and is comparable to those used in lattice Boltzmann DNS studies of rough wall turbulence (Kuwata and Kawaguchi, 2018, 2019; Kuwata et al., 2020; Kuwata and Nagura, 2020). In this simulation, we utilized the bounce-back scheme for unknown distribution functions propagating from a boundary surface. For comparison, we also performed the DNS of the turbulent heat transfer over a smooth wall at $\text{Re}_\tau = 450$. The flow conditions and simulation parameters, including the computational domain size and number of grid points, were identical to those in the rough wall cases. Note that the grid resolution of $\Delta^+ \simeq 1.8$ is sufficient to provide solutions for the turbulent channel flow, which is significantly closer to the results obtained by the spectral method (Suga et al., 2015). For the no-slip boundary and constant heat flux conditions at the rough surface, we employed the linear interpolated bounce-back method (Pan et al., 2006; Li et al., 2014), as in previous DNS studies (Kuwata and Kawaguchi, 2019; Kuwata and Nagura, 2020). The symmetric and adiabatic boundary conditions at the top boundary are satisfied by the specular reflection bounce-back (Suga et al., 2017).

2.3. Friction velocity and temperature

Unlike a flow over a smooth surface, the determination of the friction velocity and temperature for the rough surface are not straightforward because they strongly depend on the location of the origin of the rough surface. This is less important when the roughness height is negligibly lower than the boundary layer thickness. However, this is a crucial issue in the current DNS study, where the roughness height accounts for a relatively large fraction of the boundary layer thickness (Kuwata and Kawaguchi, 2019; Chan et al., 2015). In this study, we follow the definition proposed by Kuwata and Kawaguchi (2019), in which the friction velocity based on the averaged wall shear stress of the rough surface, $u_\tau = \sqrt{\tau_w^a/\rho}$, is computed from the streamwise momentum balance between the pressure drop ΔP and the wall shear stress τ_w^a :

$$\Delta P S_{yz} = \tau_w^a A, \quad (1)$$

where $A = L_x L_z$ is the reference surface area, and $S_{yz} = V_f/L_x$ is the mean $y - z$ plane area occupied by the fluid phase, where V_f is the volume of the fluid phase. Following Kuwata and Kawaguchi (2019); Kuwata and Nagura (2020), we can transform the effective area into $S_{yz} = \delta_e L_z$ using the effective half channel height δ_e . This yields

$$u_\tau = \sqrt{\frac{\Delta P \delta_e}{\rho L_x}}. \quad (2)$$

Note that τ_w^a obtained from Eq.(1) corresponds to the total shear stress at a mean surface height $y = h_m$ (Kuwata and Kawaguchi, 2019), and it is consistent with the definition provided by Forooghi et al. (2017); Chan et al. (2015).

Analogous to the wall shear stress, the friction temperature is also defined by the equivalent heat flux q_w^a as $t_\tau = q_w^a / (\rho c u_\tau)$, where q_w^a is given by the energy budget of the system as follows:

$$\int_0^{L_x} \int_0^{L_y} \int_0^{L_z} \overline{s_{cht}} dx dy dz = q_w^a A, \quad (3)$$

where c is the specific heat, and $\overline{s_{cht}}$ denotes the time-averaged source term included in the energy equation for the constant heat flux condition, as described in Appendix A. Note that the integration of $\overline{s_{cht}}$ over the system (left-hand side of Eq.(3)) analytically yields $A_r q_w$ after some calculations, where A_r is the rough surface area (see Appendix B). Thus, q_w^a is simply given as $q_w^a = \frac{A_r}{A} q_w$. In this study, we discuss the temperature variance relative to the wall temperature $\Theta = T_w - T$, where T_w and T denote the wall and fluid temperatures, respectively. Throughout this paper, the value with “+” denotes the value normalized with the friction velocity or temperature.

2.4. Rough surface

One of the objectives of this study was to clarify the effect of surface characteristics on turbulent heat transfer over a rough surface. Therefore, based on the previous systematic DNS study by Kuwata and Nagura (2020), we considered six rough surfaces in which the skewness (Sk) and effective slope (ES) values were systematically varied while the root-mean-square roughness remained fixed. The skewness Sk is defined as the statistical moment of the rough surface elevation, $h(x, z) - h_m$, expressed as follows:

$$Sk = \frac{1}{h_{rms}^3 A} \int_x \int_z (h(x, z) - h_m)^3 dx dz, \quad (4)$$

where $h(x, z)$ is the rough surface height, and h_{rms} is the root-mean-square roughness height.

$$h_{rms}^2 = \frac{1}{A} \int_x \int_z (h(x, z) - h_m)^2 dx dz. \quad (5)$$

The fourth moment of surface elevation is referred to as kurtosis, Ku , which is defined as follows:

$$Ku = \frac{1}{h_{rms}^4 A} \int_x \int_z (h(x, z) - h_m)^4 dx dz. \quad (6)$$

The parameters Sk and Ku are closely related to the shape of the PDF of the surface height. The skewness measures whether the surface of interest has a valley-dominated or peak-dominated nature, whereas Ku measures the significance of the tail of the PDF. The effective slope ES proposed by Napoli et al. (2008) is defined as the average value of the slope of the surface height:

$$ES = \frac{1}{A} \int_x \int_z \left| \frac{\partial h(x, z)}{\partial x} \right| dx dz. \quad (7)$$

The effective slope ES represents the wavelength of the surface undulations or solidity of the roughness elements (Napoli et al., 2008; Chan et al., 2015; MacDonald et al., 2016).

The rough surface considered in this study was a three-dimensional irregular rough surface with an isotropic and homogeneous nature. Although the procedure for generating a rough surface is the same as that in Kuwata and Nagura (2020), we briefly summarize our process of generating rough surfaces in which Sk and ES are systematically varied. First, we generated the original surface tile by superimposing roughness cones of various heights and widths. The roughness cone was generated by a rotating body of a hyperbolic sine function, and the shape parameters were adjusted by trial

and error such that the obtained Sk and ES values were close to the target values of $Sk = +0.53$ and $ES = 0.16$, respectively. Based on this original rough surface, we generated the other five rough surfaces with different Sk and ES values: the sign of the Sk value was changed by inverting the surface height as $h_p - h(x, z)$, where h_p is the maximum roughness peak, whereas the ES value was increased by reducing the surface width in the streamwise and spanwise directions while preserving the surface height. These transformations can be observed in Figure 2, where the rough surfaces colored by the surface elevation are shown together with the Sk and ES values. The inversion process transformed the surface peaks of the original rough surface, as shown in Fig.2(a), into surface valleys in Fig.2(d), modifying the peak-dominated surface of $Sk = +0.53$ into a valley-dominated surface with $Sk = -0.53$. Note that this transformation did not affect the values of Ku , h_{rms} , and ES . The procedure for varying the ES value is shown in Fig.2 (a,b): when the size of the original rough surface of $6\delta(x) \times 3\delta(z)$ of Fig.2 (a) was reduced by a factor of two, and 2×2 reduced tiles of $3\delta(x) \times 1.5\delta(z)$ were remapped when the domain size was fixed, the wavelength of the surface was doubled as shown in Fig.2 (b). Notably, this transformation did not affect the values of Sk , Ku , and h_{rms} , which only altered the ES value.

The characteristic parameters, including the values of Sk , ES , Ku , h_m , and h_{rms} , and the mean peak-to-valley height h_t , are summarized in Table 1, where h_t is computed by partitioning the surface in Fig.2(a) into 5×5 tiles of equal size (Thakkar et al., 2017). Inverting the surface height alters the mean roughness height h_m , while the roughness height scales of h_{rms} and h_t are fixed ($h_{rms}/\delta = 0.035$ and $h_t/\delta = 0.14$) as presented in Table 1.

The mean peak-to-valley height normalized by the effective channel height is $h_t/\delta_e \simeq 0.16$, which is close to that in previous DNS studies conducted by Thakkar et al. (2017), who demonstrated that the blockage by the wall roughness of $h_t \simeq \delta_e/6$ hardly altered the flow in the outer layer. The present rough surfaces have relatively low Sk values ($Sk = \pm 0.53$) and $Ku = 3$, suggesting that the PDF of the height elevation is relatively close to the Gaussian distribution in which the majority of the real rough surfaces are clustered (Jelly and Busse, 2019). As for the mean wavelength of the surface undulation, the range of ES values is $ES = 0.16 - 0.64$, which covers the wavy surface to rough surface regimes (Schultz and Flack, 2009).

The advantage of the procedure of reducing and inverting the rough surface is that this procedure only modified the ES and Sk values while strictly preserving the roughness height scales such as h_{rms} , h_t , and the surface height amplitude. However, strictly speaking, the transformed surfaces for $ES = 0.32$ and 0.64 cannot be regarded as perfectly irregular but have periodicity in the x and z directions. The streamwise period of the tile for $ES = 0.64$ is 1.5δ , which is not sufficiently longer than the streamwise integral scale of the velocity fluctuations. However, Kuwata and Nagura (2020) reported that the rough surfaces generated by this procedure yielded hydraulic roughness effects comparable to realistic irregular rough surfaces. Thus, the effect of periodicity of the rough surface was considered negligible.

With regard to the grid resolution, we confirm from Figure 3 that the current grid resolution is sufficiently fine to resolve the roughness geometry even for the case with $ES = 0.64$ where the wavelength of the surface undulations is the smallest. Furthermore, a grid sensitivity study was also performed for

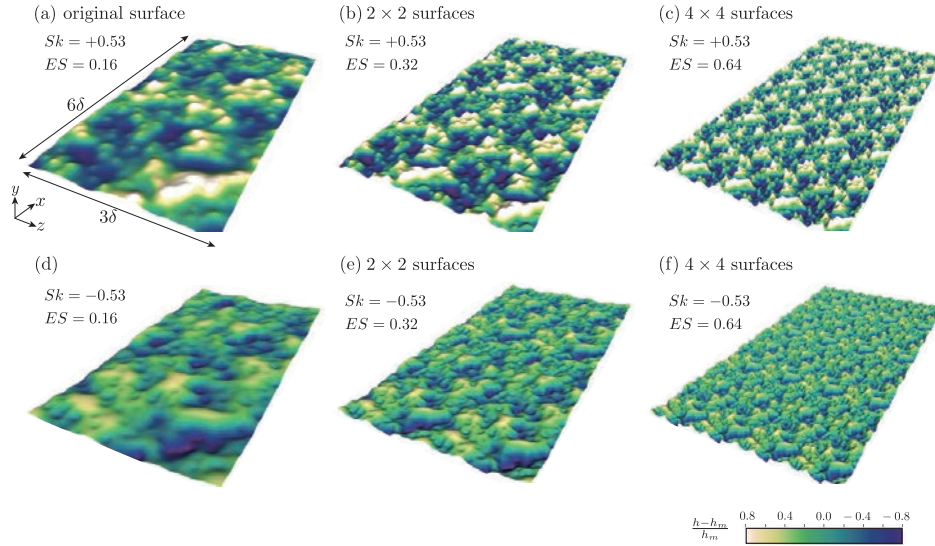


Figure 2: Three-dimensional irregular rough surfaces colored by the surface elevation $(h - h_m)/h_m$: (a) original surface with $Sk = +0.53$ and $ES = 0.16$, (b) surface with $Sk = +0.53$ and $ES = 0.32$, (c) surface with $Sk = +0.53$ and $ES = 0.64$, (d) surface with $Sk = -0.53$ and $ES = 0.16$, (e) surface with $Sk = -0.53$ and $ES = 0.32$, and (f) surface with $Sk = -0.53$ and $ES = 0.64$.

the case with $ES = 0.64$ and $Sk = +0.53$, and we have confirmed that doubling the grid resolution yields a change in the skin friction coefficient and Stanton number of 0.5% and 1.6%, respectively. Hence, the grid resolution employed in this study can not only correctly resolve the roughness geometry but also capture fine-scale turbulent dynamics near the rough wall.

Table 1: Characteristic parameters of rough surfaces; Sk is the skewness, ES is the effective slope, Ku is the kurtosis, h_m is the mean roughness height, h_{rms} is the root-mean-square roughness, h_t is the mean peak-to-valley height, and δ_e is the effective channel height.

Symbol	Sk	ES	Ku	h_m/δ	h_{rms}/δ	h_t/δ	h_t/δ_e	δ_e/δ
—○—	+0.53	0.16	3.0	0.075	0.035	0.14	0.16	0.926
—△—	+0.53	0.32	3.0	0.075	0.035	0.14	0.16	0.926
—△—	+0.53	0.64	3.0	0.075	0.035	0.14	0.16	0.926
—●—	-0.53	0.16	3.0	0.12	0.035	0.14	0.17	0.876
—▲—	-0.53	0.32	3.0	0.12	0.035	0.14	0.17	0.876
—■—	-0.53	0.64	3.0	0.12	0.035	0.14	0.17	0.876

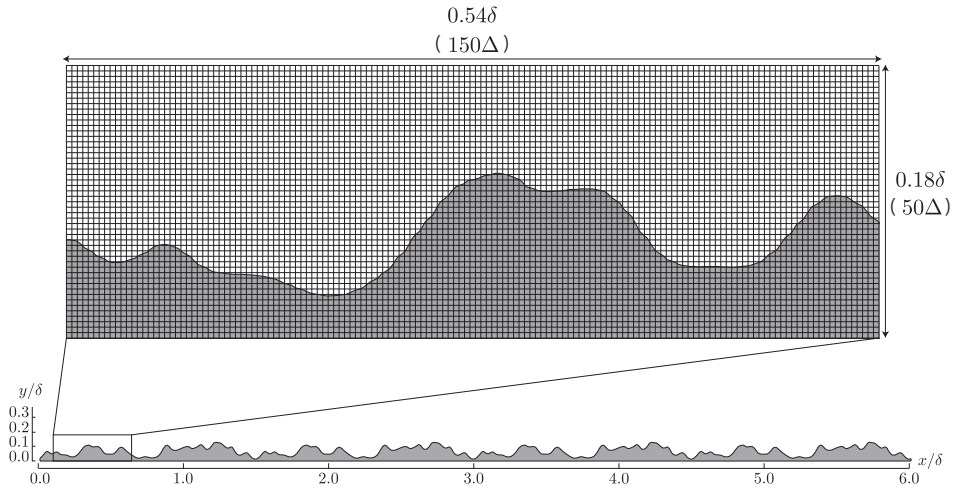


Figure 3: Grid arrangement for the case with $ES = 0.64$ and $Sk = +0.53$ where the wavelength of the surface undulations is the smallest.

2.5. Averaging procedure

To statistically discuss turbulence near a rough wall where a time-averaged variable changes in space owing to the presence of a rough surface, we employed a double-averaging methodology consisting of spatial- and time-averaging operators. For spatial averaging, superficial and intrinsic $x - z$ plane-averaging methods were introduced (Kuwata et al., 2020; Kuwata and Nagura, 2020; Kuwata and Kawaguchi, 2019). The superficial averaging of a variable $\phi(x, y, z)$ is defined as follows:

$$\langle \phi \rangle(y, t) = \frac{1}{A} \int_x \int_z \phi(x, y, z, t) dx dz. \quad (8)$$

The intrinsic averaging is taken over the fluid phase in the $x - z$ plane as follows:

$$\langle \phi \rangle^f(y, t) = \frac{1}{A_f} \int_x \int_z \phi(x, y, z, t) dx dz, \quad (9)$$

where A_f is the fluid phase area within the $x - z$ plane, and the superficial and intrinsic averaged values are related through the plane porosity $\varphi = A_f/A$ as $\langle \phi \rangle = \varphi \langle \phi \rangle^f$. The variable $\phi(x, y, z, t)$ can be decomposed into a contribution from an intrinsic averaged value $\langle \phi \rangle^f(y, t)$ and a deviation from the intrinsic averaged value $\tilde{\phi}(x, y, z, t)$, referred to as the dispersion, as follows:

$$\phi(x, y, z, t) = \langle \phi \rangle^f(y, t) + \tilde{\phi}(x, y, z, t). \quad (10)$$

The Reynolds decomposition is also introduced to the time-dependent variable $\phi(x, y, z, t)$ as follows:

$$\phi(x, y, z, t) = \bar{\phi}(x, y, z) + \phi'(x, y, z, t), \quad (11)$$

where $\phi'(x, y, z, t)$ denotes the fluctuation from the time-averaged value of $\bar{\phi}(x, y, z)$. For time averaging, the statistical properties were assembled over

a period of $60T$, where $T = L_x/U_b$ is the flow-through time, and U_b is the bulk mean velocity.

3. Results and discussion

3.1. Mean profiles

The roughness effect on the inner-scaled mean velocity and temperature with logarithmic scaling is shown in Figure 4, where the effective wall-normal distance

$$y_e = \int_0^y \varphi dy, \quad (12)$$

proposed by Kuwata and Kawaguchi (2019) is used as the distance from the rough wall. The effective distance y_e is zero at the bottom of the deepest valley, but returns to $y - h_m$ above the rough surface (Kuwata and Kawaguchi, 2019). Hence, above the rough surface, the effective distance is regarded as the normal distance from the virtual origin of $y = h_m$, as in previous studies (Chan et al., 2015; Forooghi et al., 2017). For comparison, the DNS results for the smooth-wall turbulent channel flow from Kawamura et al. (1998) were included. Fig.4(a,c) confirms that the predicted smooth wall results agree quite well with the reference data, suggesting that the present grid resolution is sufficient to reasonably resolve fine-scale near-wall eddies. The slight discrepancy away from the wall is attributed to the difference in the flow configuration. This study considers an open-channel flow with symmetric boundary conditions at the channel center, whereas the full-channel flow was simulated for the reference DNS by Kawamura et al. (1998). For the rough surface cases, both the mean velocity and temperature profiles are shifted

downward from the smooth wall results due to the enhancement of momentum and heat transfer by the rough surfaces. In addition, the figure shows that the profiles away from the wall appear to maintain a logarithmic profile. However, as shown in Figure 5, where the mean velocity and temperature defect profiles are compared, the similarity in the logarithmic region cannot be perfectly preserved even away from rough surfaces. This is due to the fact that for the current rough surfaces, the roughness height relative to the channel height is not sufficiently small (Jiménez, 2004; Schultz and Flack, 2005; Flack et al., 2007; Flack and Schultz, 2014). Fig.4(a,b) shows that the downward shift in $\langle \bar{u} \rangle^+$ is pronounced for the surface with the positive Sk and larger ES values, which is consistent with the previous DNS studies (Napoli et al., 2008; Chan et al., 2015; De Marchis et al., 2010; Flack and Schultz, 2010; Flack et al., 2020). A similar trend is apparent for the downward shift in $\langle \bar{\theta} \rangle^+$, as shown in Fig.4(c,d). However, the downward shifts in $\langle \bar{\theta} \rangle^+$ are found to be somewhat smaller than those in $\langle \bar{u} \rangle^+$.

To clarify the relationship between the downward shifts in $\langle \bar{\theta} \rangle^+$ and $\langle \bar{u} \rangle^+$, Figure 6 depicts the roughness function ΔU^+ and $\Delta \Theta^+$, which is evaluated as the difference in the mean profiles at $y_e^+ \simeq 100$ with the smooth-wall results (Kuwata and Kawaguchi, 2019; Kuwata and Nagura, 2020). In addition, the DNS data for three-dimensional irregular roughness at $Pr = 1$ from Peeters and Sandham (2019) and three-dimensional sinusoidal roughness at $Pr = 0.7$ from MacDonald et al. (2019) are shown. The roughness function ΔU^+ exhibits the maximum value of $\Delta U^+ = 9.7$ for the case with $Sk = +0.53$ and $ES = 0.64$ followed by the case with $Sk = +0.53$ and $ES = 0.32$ and $Sk = -0.53$ and $ES = 0.64$, and is the smallest for the case with

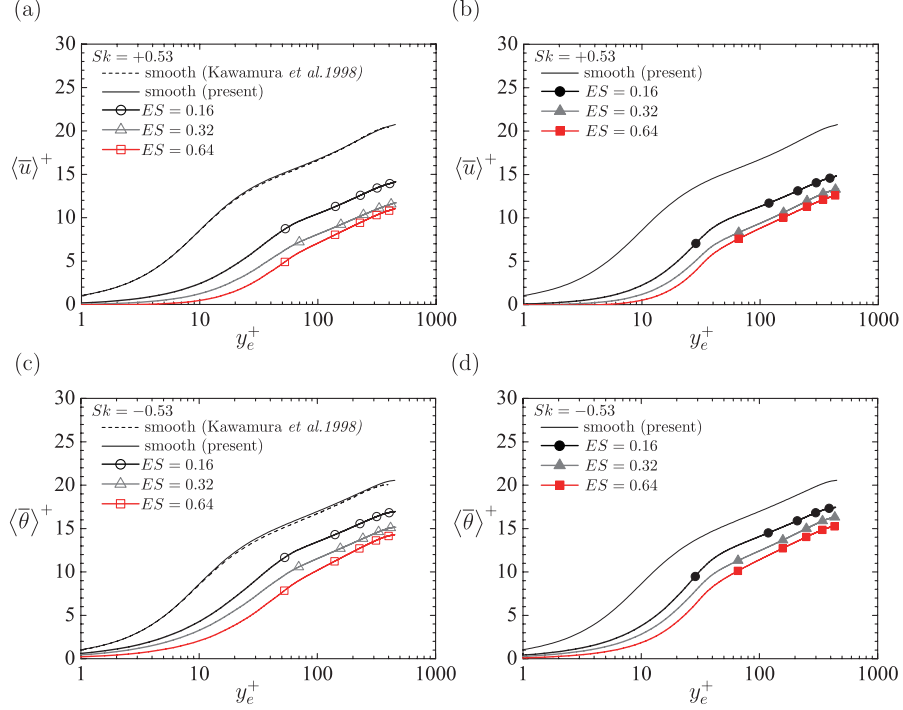


Figure 4: Comparison of the mean profiles with logarithmic scaling: (a) mean velocity for $Sk = +0.53$, (b) mean velocity for $Sk = -0.53$, (c) mean temperature for $Sk = +0.53$, and (d) mean temperature for $Sk = -0.53$. The DNS results for the smooth-wall turbulent channel flow from Kawamura et al. (1998) are also shown.

$Sk = -0.53$ and $ES = 0.16$. Based on the criterion of the fully rough regime of $\Delta U^+ \gtrsim 7 (k_s^+ > 70)$ proposed by Nikuradse (1933), the simulated flows can be categorized as a fully rough regime, except for the cases with $ES = 0.16$. The figure also shows that $\Delta \Theta^+$ is consistently smaller than ΔU^+ , irrespective of the Sk and ES values. Interestingly, the trend of the present results is similar to that of the three-dimensional irregular rough surface of Peeters and Sandham (2019), but deviates from the sinusoidal roughness of MacDonald et al. (2019) when $\Delta U^+ > 7$. The reason for the

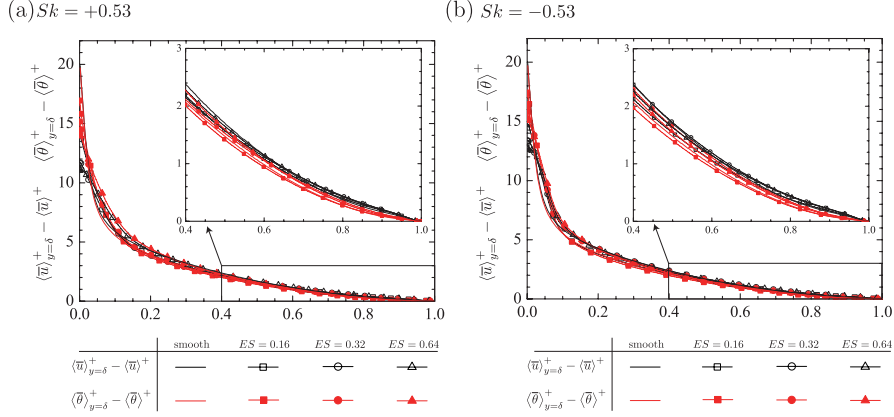


Figure 5: Comparison of the mean velocity and temperature profiles with defect form: (a) for case $Sk = +0.53$, (b) for case $Sk = -0.53$.

deviation is not clear. However, it may be responsible for the differences in the roughness structure and molecular Prandtl number.

To better understand the physical meaning of the relation $\Delta U^+ > \Delta \Theta^+$, we attempt to derive the relation among the Reynolds analogy factor and roughness functions. The inner-scaled mean velocity and temperature profiles in the log-law region can be expressed as follows:

$$\langle \bar{u} \rangle^+ = \frac{1}{\kappa} \ln(y_e^+) + B - \Delta U^+, \quad (13)$$

$$\langle \bar{\theta} \rangle^+ = \frac{Pr_t}{\kappa} \ln(y_e^+) + \beta(Pr) - \Delta \Theta^+, \quad (14)$$

where Pr_t is the turbulent Prandtl number, and κ is the von Kármán constant. The values for B and $\beta(Pr)$ are the log-law intercepts of the mean velocity and temperature, respectively (Kader, 1981). Integrations of Eqs. (13) and (14) over 0 to δ_e^+ divided by δ_e^+ yield the inner-scaled bulk mean

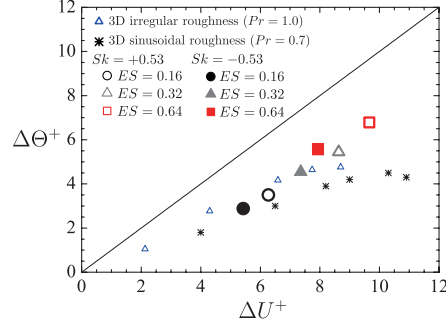


Figure 6: Velocity and temperature roughness functions. The DNS data for the three-dimensional irregular roughness from Peeters and Sandham (2019) and three-dimensional sinusoidal roughness from MacDonald et al. (2019) are included. The black thin line indicates $\Delta\Theta^+ = \Delta U^+$.

velocity and arithmetic mean temperature as follows:

$$U_b^+ \simeq \frac{1}{\delta_e^+} \int_0^{\delta_e^+} \langle \bar{u} \rangle^+ dy_e^+ = \frac{1}{\kappa} \ln(Re_\tau) - \frac{1}{\kappa} + B - \Delta U^+, \quad (15)$$

$$\Theta_a^+ \simeq \frac{1}{\delta_e^+} \int_0^{\delta_e^+} \langle \bar{\theta} \rangle^+ dy_e^+ = \frac{Pr_t}{\kappa} \ln(Re_\tau) - \frac{Pr_t}{\kappa} + \beta(Pr) - \Delta\Theta^+. \quad (16)$$

The global flow resistance and heat transfer rate can be quantified by the skin friction coefficient C_f and the Stanton number S_t : which can be, respectively, expressed as follows:

$$C_f = \frac{2}{(U_b^+)^2}, \quad S_t = \frac{1}{U_b^+ \Theta_m^+}, \quad (17)$$

where Θ_m^+ denotes the bulk (mixed-mean) temperature, which is related to Θ_a^+ as follows (MacDonald et al., 2019):

$$\Theta_m^+ = \Theta_a^+ + \frac{Pr_t}{\kappa^2 U_b^+}. \quad (18)$$

Equations (15), (16), (17), and (18) yield the Reynolds analogy factor $RA =$

$(2S_t)/C_f$ as follows:

$$RA = \frac{1}{Pr_t + \sqrt{0.5C_f f_k}}, \quad (19)$$

$$f_k = Pr_t \Delta U^+ - \Delta \Theta^+ + \beta(Pr) - Pr_t B + \frac{Pr_t}{\kappa^2} \sqrt{0.5C_f}. \quad (20)$$

For the current simulations ($Pr = 1$ and $Re_\tau = 450$), the predicted mean velocity and temperature profiles almost collapse onto each other, which indicates that the slope and intercept values for the logarithmic mean velocity profile are close to the corresponding values for the logarithmic mean temperature profile. Hence, in this study, we assume that $Pr_t \simeq 1$ and $\beta(Pr) \simeq B$. Hence, RA for the present flow conditions is expressed simply as follows:

$$RA \simeq \frac{1}{1 + \sqrt{0.5C_f f_k}}, \quad f_k = \Delta U^+ - \Delta \Theta^+ + \frac{\sqrt{0.5C_f}}{\kappa^2}. \quad (21)$$

The important implications of Eq.(21) shows that RA is lower than unity when $\Delta U^+ > \Delta \Theta^+$ (i.e., $f_k > 0$). Thus, the observation $\Delta U^+ > \Delta \Theta^+$ in Fig.6 indicates the breakdown of the Reynolds analogy; that is, the momentum transfer augmentation is more significant than the heat transfer augmentation. This is consistent with the observation that the Reynolds analogy does not hold for rough wall turbulence (Kato et al., 2000; Bons, 2002; Nagano et al., 2004; Forooghi et al., 2018a; Peeters and Sandham, 2019; MacDonald et al., 2019). For predictive correlation for S_t for rough wall turbulence, Dipprey and Sabersky (1963) semi-analytically derived the same expression of Eq. (19), and an empirical correlation for f_k was derived via experiments on sand-grain roughness as $f_k = 5.19(k_s^+)^{0.2} Pr^{0.44} - 8.48$ with $Pr_t = 1.0$. Kays and Crawford (1993) proposed the other expression for $f_k = (k_s^+)^{0.2} Pr^{0.44}/C$ with a constant of $C = 1.0$. The experimentally

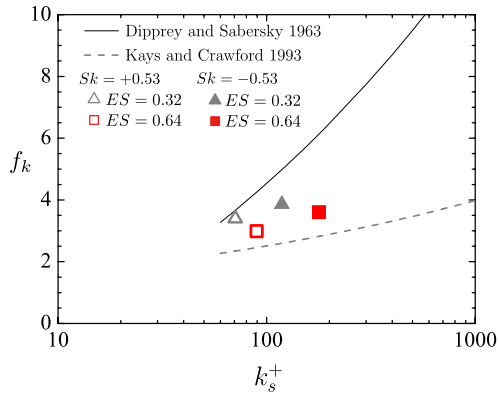


Figure 7: Correlation of the function f_k against the inner-scaled equivalent sand-grain roughness. The present DNS data in the fully rough regime $ES = 0.32$ and $ES = 0.64$ together with data from Peeters and Sandham (2019), the experimental correlations $f_k = 5.19(k_s^+)^{0.2}Pr^{0.44} - 8.48$ by Dipprey and Sabersky (1963), and $f_k = (k_s^+)^{0.2}Pr^{0.44}/C$ with a constant $C = 1.0$ by Kays and Crawford (1993).

derived correlations f_k obtained by Dipprey and Sabersky (1963); Kays and Crawford (1993) are compared with the present DNS data in Figure 7. Note that the present results are shown only for cases in the fully rough regime, where the equivalent sand-grain roughness height k_s^+ can be estimated by the following relation (Flack and Schultz, 2010):

$$k_s^+ = \exp [\kappa (8.5 - B + \Delta U^+)]. \quad (22)$$

where the von Kármán constant $\kappa = 0.4$ and the log-law intercept for a smooth $B = 5.2$ were used. As shown in the figure, f_k by Dipprey and Sabersky (1963) is generally larger than that by Kays and Crawford (1993), indicating that f_k by Dipprey and Sabersky (1963) predicts a stronger dissimilarity between momentum and heat transfer because a larger f_k value leads to a smaller RA value in Eq.(21). It is observed that the present DNS

results lie between the two correlation functions, and we cannot assert which correlation yields a better prediction for the present DNS data. Further investigation at a higher Reynolds number flow is required to answer this question.

Besides those correlations for RA proposed by Dipprey and Sabersky (1963); Kays and Crawford (1993), other correlation functions that predict RA have been proposed so far. In this study, three prediction functions are used for a comparison:

$$RA = \frac{1}{5\sqrt{0.5C_f} [Pr + \ln(1 + 5Pr) + 0.5\ln(\frac{Re}{60}\sqrt{0.5C_f})]}, \quad (23)$$

from Martinelli (1947).

$$RA = \frac{1}{1 + 1.5Re^{-1/8}Pr^{-1/6} \left(Pr \frac{C_f}{C_{f0}} - 1 \right)}, \quad (24)$$

from Nunner (1956).

$$RA = RA_0 \left[0.55 + 0.45\exp\left(-\frac{k_s^+}{130}\right) \right], \quad (25)$$

from Forooghi et al. (2018a).

Note that these functions are not expressed in the form of Eq.(19); however, they were all designed to provide smaller RA values by increasing the roughness effect on the flow, as in the correlations proposed by Dipprey and Sabersky (1963); Kays and Crawford (1993). In these equations, the roughness effect on the flow is represented by the equivalent sand-grain roughness k_s^+ (Forooghi et al., 2018a) or C_f at the rough surface (Martinelli, 1947; Nunner, 1956).

A comparison of the S_t predicted by the functions proposed by Dipprey and Sabersky (1963); Kays and Crawford (1993); Martinelli (1947); Nunner

(1956); Forooghi et al. (2018a) with the present DNS data is summarized in Table 2. Note that k_s^+ is unknown for the cases with $ES = 0.16$, which is considered to be located in the transitionally rough regime; thus, the results from Dipprey and Sabersky (1963); Kays and Crawford (1993); Forooghi et al. (2018a) are not shown in these cases. As presented in Table 2, the RA for the present DNS tends to be smaller for the cases with positive Sk and larger ES values, which substantiates the decrease in RA with increasing roughness effect on the flow. A comparison of the prediction functions reveals that the S_t is considerably underpredicted by the functions proposed by Martinelli (1947); Nunner (1956), whereas the predictions using the functions proposed by Dipprey and Sabersky (1963); Kays and Crawford (1993); Forooghi et al. (2018a) show reasonable agreement with the present results with an accuracy of 15%. Notably, the agreement with the prediction using the function proposed by Forooghi et al. (2018a) indicates that the RA correlates well with a single parameter of the inner-scaled equivalent sand roughness, despite the considerable variation in the Sk and ES values, which strongly supports the findings of Forooghi et al. (2018a).

Table 2: Comparison of the predicted Reynolds analogy factor with the DNS data. The Dipprey function of $f_k = 5.19(k_s^+)^{0.2}Pr^{0.44} - 8.48$ using Eq.(21), and $Pr_t = 1$ from Dipprey and Sabersky (1963); The Kays function of $f_k = (k_s^+)^{0.2}Pr^{0.44}/C$ with Eq.(21) and $C = 1$ from Kays and Crawford (1993); Eq.(23) from Martinelli (1947); Eq.(24) from Nunner (1956); and Eq.(25) from Forooghi et al. (2018a) are compared.

Sk	ES	RA	Dipprey (present) function	Kays function	Eq.(23)	Eq.(24)	Eq.(25)
+0.53	0.16	0.77	-	-	-27%	-21%	-
+0.53	0.32	0.69	-6%	+13%	-35%	-38%	+6%
+0.53	0.64	0.67	-14%	+11%	-40%	-46%	-1%
-0.53	0.16	0.79	-	-	-24%	-17%	-
-0.53	0.32	0.74	+1%	+11%	-30%	-28%	+10%
-0.53	0.64	0.74	-5%	+8%	-35%	-35%	+5%

3.2. Momentum and energy budgets

The previous section focused on global quantities to discuss the augmentation of heat and momentum transfer. To clarify the underlying physics better, this subsection focuses on the effects of roughness on the heat and momentum transfer mechanisms by analyzing the double-averaged equations. Applying the spatial- ($x - z$ plane) and time-averaging operators to the Navier–Stokes equation for incompressible flows, we can obtain the double-averaged momentum equation as follows:

$$\begin{aligned} \langle \bar{u}_j \rangle \frac{\partial \langle \bar{u}_i \rangle^f}{\partial x_j} &= -\frac{\varphi}{\rho} \frac{\partial \langle \bar{p} \rangle^f}{\partial x_i} + \frac{\partial}{\partial x_j} \left(\nu \frac{\partial \langle \bar{u}_i \rangle}{\partial x_j} \right) - \frac{\partial}{\partial x_j} \left(\underbrace{\langle \tilde{u}_i \tilde{u}_j \rangle}_{\mathcal{T}_{ij}} + \underbrace{\langle u'_i u'_j \rangle}_{R_{ij}} \right) \\ &\quad - \underbrace{\frac{1}{\rho A} \int_L \bar{p} n_i d\ell_y}_{\bar{f}_{p_i}} - \underbrace{\frac{\nu}{A} \int_L \left(-n_j \frac{\partial \bar{u}_i}{\partial x_j} \right) d\ell_y}_{\bar{f}_{v_i}}, \end{aligned} \quad (26)$$

where L represents the obstacle perimeter within an averaging $x - z$ plane, ℓ_y represents the length defined as $\ell_y = \partial A_r / \partial y$, and n_k is its unit normal vector pointing outward from the fluid to the solid phase. The second moments are the $x - z$ plane-averaged Reynolds stress R_{ij} and a plane-dispersive covariance \mathcal{T}_{ij} , which arises owing to the inhomogeneous nature of the mean flow in the $x - z$ plane. The time-averaged viscous and pressure drag force terms (\bar{f}_{v_i} and \bar{f}_{p_i} , respectively) are expressed as the averaged pressure dispersion and viscous stress over the obstacle perimeter at a certain plane, respectively. Note that the viscous drag can be split into contributions of the velocity dispersion and mean shear, as in Kuwata and Kawaguchi (2019):

$$\bar{f}_{v_i} = \frac{\nu}{A} \int_L \left(-n_j \frac{\partial \tilde{u}_i}{\partial x_j} \right) d\ell_y + \nu \frac{\partial \varphi}{\partial x_j} \frac{\partial \langle \bar{u}_i \rangle^f}{\partial x_j}. \quad (27)$$

However, we ignore this decomposition for simplicity. By integrating Eq. (26) over the wall-normal direction from 0 to y and normalizing by u_τ^2 , the stress balance for the present flow system in non-dimensional form can be derived after some manipulation (Kuwata and Kawaguchi, 2019):

$$1 - \frac{y_e}{\delta_e} = \frac{\partial \langle \bar{u} \rangle^+}{\partial y^+} - R_{12}^+ - \mathcal{T}_{12}^+ + \underbrace{\int_{y^+}^{h_p^+} \overline{f_{v_x}^+} dy^+}_{Fv_x^+} + \underbrace{\int_{y^+}^{h_p^+} \overline{f_{p_x}^+} dy^+}_{Fp_x^+}, \quad (28)$$

where Fv_x^+ and Fp_x^+ denote the contributions of the viscous and pressure drag terms, respectively.

Similar to the momentum equation, the double-averaged energy equation in a non-dimensional form can be derived as follows:

$$\begin{aligned} \langle \bar{u}_j \rangle \frac{\partial \langle \bar{\theta} \rangle^f}{\partial x_j} &= \frac{\partial}{\partial x_j} \left(\alpha \frac{\partial \langle \bar{\theta} \rangle}{\partial x_j} \right) - \frac{\partial}{\partial x_j} \left(\underbrace{\langle \theta' u_j' \rangle}_{H_j} + \underbrace{\langle \tilde{\theta} \tilde{u}_j \rangle}_{\mathcal{H}_j} \right) \\ &\quad - \underbrace{\frac{\alpha}{A} \int_L \left(-n_j \frac{\partial \bar{\theta}}{\partial x_j} \right) dl_y}_{\overline{s_w}^+} - \underbrace{\frac{\alpha}{A} \frac{\partial}{\partial x_j} \left(\int_L n_j \bar{\theta} dl_y \right)}_{\overline{s_t}^+} + \langle \overline{s_{cht}} \rangle, \end{aligned} \quad (29)$$

where H_j and \mathcal{H}_j are the $x-z$ plane-averaged turbulent heat flux and plane-dispersion heat flux, respectively, and s_{cht} is the source term included to impose constant heat flux conditions for the rough surface (See Appendix A for the derivation of s_{cht}). The time-averaged wall interaction terms ($\overline{s_w}$ and $\overline{s_t}$) are the wall heat transfer and tortuosity molecular diffusion terms, respectively, (Kuwahara et al., 1996). Note that $\overline{s_t}$ is zero in the present simulation because the temperature variance at the rough surface is zero from the definition.

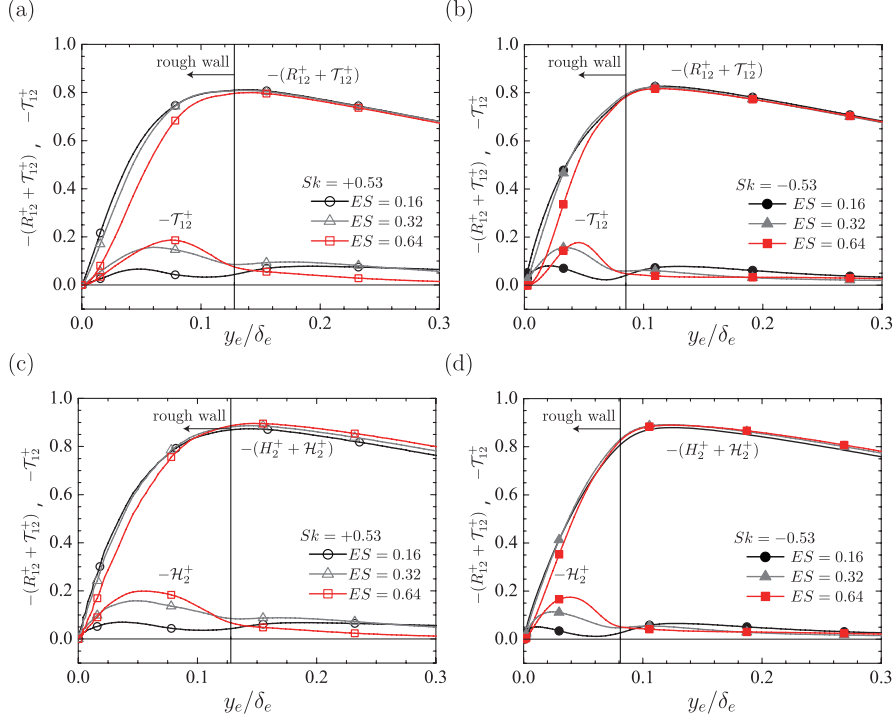


Figure 8: (a) R_{12}^+ and \mathcal{T}_{12}^+ for cases with $Sk = +0.53$, (b) R_{12}^+ and \mathcal{T}_{12}^+ for cases with $Sk = -0.53$, (c) H_2^+ and \mathcal{H}_2^+ for cases with $Sk = +0.53$, and (d) H_2^+ and \mathcal{H}_2^+ for cases with $Sk = -0.53$. The black thin line indicates the location of the maximum roughness crest.

By integrating Eq. (29) over the wall-normal direction from 0 to y and normalizing by $t_\tau u_\tau$, The heat flux balance in a non-dimensional form can also be derived as follows:

$$1 - \frac{1}{\delta_e} \int_0^y \frac{\langle \bar{u} \rangle}{U_b} dy = \frac{1}{Pr} \frac{\partial \langle \bar{\theta} \rangle^+}{\partial y^+} - H_2^+ - \mathcal{H}_2^+ + \underbrace{\int_{y^+}^{h_p^+} \frac{s_w^+}{s_w^+} dy^+}_{H_w^+} \quad (30)$$

where the wall heat transfer contribution is denoted as H_w^+ . See Appendix B for a detailed derivation of the double-averaged heat-flux balance equation.

In the following, the momentum budgets and related terms are shown

as a function of the effective wall-normal distance y_e . As the total stress is consistently expressed as $1 - y_e/\delta_e$ on the left-hand side of Eq.(28) irrespective of the geometry of rough surfaces, the use of y_e/δ_e makes it easier to compare the momentum budgets for different rough surfaces. In addition, it is interpreted using Eq.(12) that y_e is the weighted wall-normal distance with respect to the porosity (void fraction) in the $x - z$ plane. That is, y_e effectively shrinks the region where the porosity is so small that the changes in the momentum budgets are considerably small. Indeed, Kuwata et al. (2020); Kuwata and Kawaguchi (2019) reported that the use of y_e enables us to scale the turbulence statistics near rough surfaces better than the normal distance from the mean surface height $y - h_m$.

The plane-averaged Reynolds and plane-dispersive shear stresses (R_{12}^+ and \mathcal{T}_{12}^+ , respectively, in Eq.(28)) are shown in Figure 8 (a,b), whereas the turbulent and dispersion heat fluxes (H_2^+ and \mathcal{H}_2^+ , respectively, in Eq.(30)) are shown in Fig.8 (c,d). In Fig.8(a,b), the dispersive shear stress $-\mathcal{T}_{12}^+$ is pronounced below the maximum roughness crest and increases with the ES value. Conversely, although the results are not shown here, $-R_{12}^+$ decreases with the ES value. Consequently, $-(R_{12}^+ + \mathcal{T}_{12}^+)$ is almost unchanged when the ES value increases from 0.16 to 0.32, whereas it slightly decreases below the maximum roughness crest when the ES value further increases from 0.32 to 0.64. This observation is consistent with the findings of Kuwata and Nagura (2020), who concluded that the wall roughness with a larger ES value prevents the formation of quasi-streamwise elongated vortices, leading to the considerable reduction in $-R_{12}^+$. An analogous trend can be observed for heat transfer in Fig.8(c,d): the dispersion heat flux $-\mathcal{H}_2^+$ below the max-

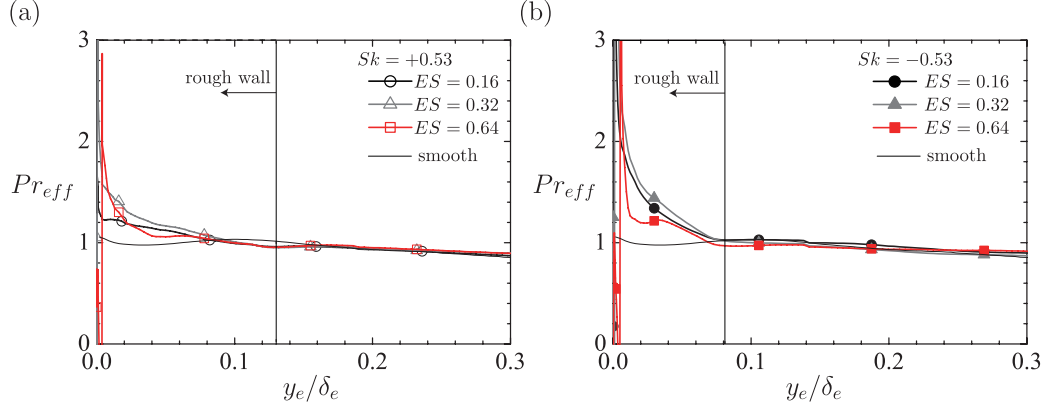


Figure 9: Effective Prandtl number: (a) for cases with $Sk = +0.53$, and (b) for cases with $Sk = -0.53$. The black thin line indicates the location of the maximum roughness crest.

imum roughness crest increases with the ES value, whereas the sum of the heat fluxes, $-(H_2^+ + \mathcal{H}_2^+)$, decreases below the roughness crest when the ES value increases from 0.32 to 0.64.

An important quantity in discussing the Reynolds analogy between momentum and heat transfer is the effective Prandtl number. It is defined as the ratio of the momentum and heat transfer diffusivities, including the effects of turbulence and dispersion:

$$Pr_{eff} = \frac{\nu_{eff}}{\alpha_{eff}} = \frac{-(R_{12} + \mathcal{T}_{12}) / \left(\frac{\partial \langle \bar{u} \rangle}{\partial y} \right)}{-(H_2 + \mathcal{H}_2) / \left(\frac{\partial \langle \bar{\theta} \rangle}{\partial y} \right)}. \quad (31)$$

Note that $Pr_{eff} \simeq Pr_t$ away from the rough wall, where the plane-dispersive shear stress (plane-dispersion heat flux) becomes negligible compared with the plane-averaged Reynolds shear stress (plane-averaged turbulent heat flux). The profiles of the effective Prandtl number Pr_{eff} are shown in Figure 9. For comparison, Pr_t for the smooth-wall case is also shown. It is observed that the effect of the wall roughness on Pr_{eff} is confined below the

maximum roughness crest: Pr_{eff} below the maximum roughness crest of $0.01 < y_e/\delta_e < 0.08$ is generally larger than that of the smooth wall, which is consistent with the observations by Peeters and Sandham (2019); Crimaldi et al. (2006); Nagano et al. (2004). This indicates that the effective thermal diffusivity is smaller than the effective eddy diffusivity, and this is considered to be one of the reasons for the dissimilarity between momentum and heat transfer, as discussed in §3.1. The reason for the rise in Pr_{eff} within the rough wall of $0.01 < y_e/\delta_e < 0.08$ can be found in the contour maps of $-\overline{u'v'}^+$ and $-\overline{v'\theta'}^+$ in Figure 10. It is apparent from Fig.10 that $-\overline{u'v'}^+$ and $-\overline{v'\theta'}^+$ show generally a similar trend; however, a distinct difference between $-\overline{u'v'}^+$ and $-\overline{v'\theta'}^+$ can be partially observed just behind the roughness crests, where $-\overline{v'\theta'}^+$ is somewhat smaller than $-\overline{u'v'}^+$. A similar trend can also be reported by Peeters and Sandham (2019), who concluded that this is due to the presence of recirculation zones behind the roughness crest, which had a detrimental effect on heat transfer. The underlying mechanisms of the dissimilarity may be responsible for the fundamental difference between the flow and scalar fields. In a series of studies on dissimilar control by traveling waves of blowing and suction by Kasagi et al. (2010); Hasegawa and Kasagi (2011); Yamamoto et al. (2013); Kaithakkal et al. (2020), it was concluded that the flow field was coupled with the continuity constraint, whereas there was no such restriction on a scalar field which resulted in a difference in the response of the vector and scalar fields to wall manipulation. Specifically, Kaithakkal et al. (2020) reported that the local pressure gradient due to blowing and suction accelerated or decelerated the velocity but had no direct influence on the scalar fields. Note that the abrupt increase and decrease in Pr_{eff} in

the vicinity of the bottom ($y_e/\delta_e < 0.01$) is attributed to the effective eddy diffusivity ν_{eff} . In this region, the local equilibrium state of turbulence is no longer hold; the enhanced pressure diffusion serves as an energy source near the bottom of the rough surface (Dwyer et al., 1997; Ikeda and Durbin, 2007; Yuan and Piomelli, 2014; Kuwata and Suga, 2016), and this leads to an enhancement of the wall-normal Reynolds stress and the Reynolds shear stress. Owing to the role of the diffusion terms near the bottom of the rough surface, the sum of the second moments, $(R_{12} + \mathcal{T}_{12})$, has a non-zero value even in the region where the mean velocity gradient is considerably small. Consequently, the effective eddy diffusivity, which is defined as $-(R_{12} + \mathcal{T}_{12})$ divided by $\frac{\partial \langle \bar{u} \rangle}{dy}$, does not exhibit a physically meaningful value. To obtain meaningful value of Pr_{eff} in the recirculating flow region, the different definition for Pr_{eff} would be preferred (Spalart and Strelets, 2000; Peeters and Sandham, 2019).

Fig.8(a,b) shows that the sum of the second moments is significantly reduced owing to the flow blockage effects caused by the wall roughness. Alternatively, the momentum transfer in this region is compensated by the drag forces (Kuwata et al., 2020; Kuwata and Nagura, 2020; Kuwata and Kawaguchi, 2019) as shown in Figure 11, where the viscous and pressure drag contributions Fv_x^+ and Fp_x^+ , respectively, in Eq.(28) are shown. Note that the sum of the intercept values of Fv_x^+ and Fp_x^+ at $y_e = 0$ is unity because the momentum budget on the right-hand side of Eq.(28) vanishes at $y_e = 0$, except for Fv_x^+ and Fp_x^+ . Hence, we can derive the relation $\tau_w^a = \rho Fv_x(y_e = 0) + \rho Fp_x(y_e = 0)$ from Eq.(28), indicating the intercept values of Fv_x^+ and Fp_x^+ correspond to the viscous and pressure contributions

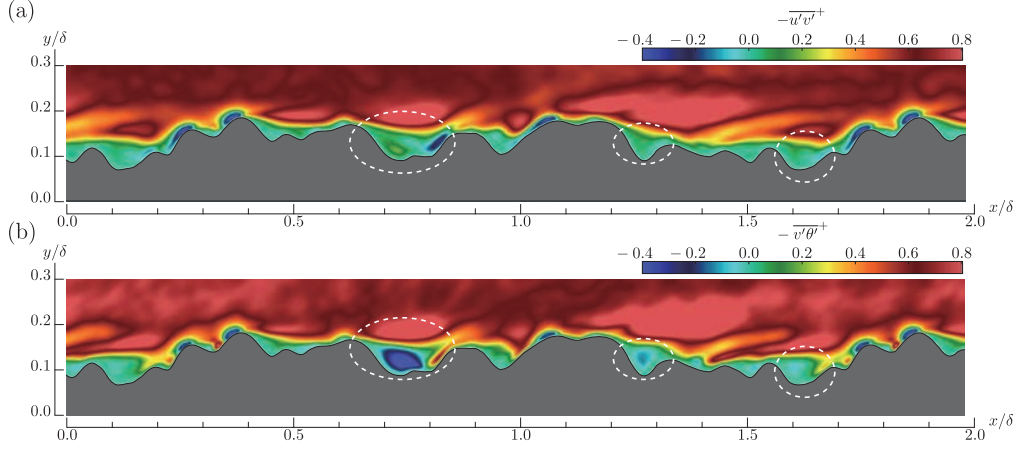


Figure 10: Contour maps of $-\overline{u'v'}^+$ and $-\overline{v'\theta'}^+$ in a $x - y$ plane for $Sk = -0.53$ and $ES = 0.64$; (a) $-\overline{u'v'}^+$, and (b) $-\overline{v'\theta'}^+$. White dashed lines indicate the region where the difference between $-\overline{u'v'}^+$ and $-\overline{v'\theta'}^+$ is apparent.

to the averaged wall shear stress, respectively. As the ES value increases, Fv_x^+ in Fig.11(a,b) near the bottom decreases, whereas the pressure drag Fp_x^+ in Fig.11(c,d) considerably increases. Consequently, for the surface with a larger ES value, the momentum transfer near the bottom is dominated by the pressure drag. This trend is consistent with the findings of Napoli et al. (2008); Kuwata and Nagura (2020).

Analogous to the momentum budgets, the reduction in the turbulent and dispersion heat fluxes near the bottom is compensated by the wall heat transfer term as shown in Figure 12 where the wall heat transfer term, $\overline{s_w}^+$, and its contribution to the total heat flux, H_w^+ , are shown. Fig.12 (a,b) shows that, as the ES value increases, $\overline{s_w}^+$ near the bottom ($y_e/\delta_e < 0.02$) decreases, but it increases away from the bottom ($y_e/\delta_e > 0.02$). The reduction in $\overline{s_w}^+$ near the bottom is considered to be due to the presence of an insulation layer in which the scalar mixing by the turbulent and dispersion heat fluxes is con-

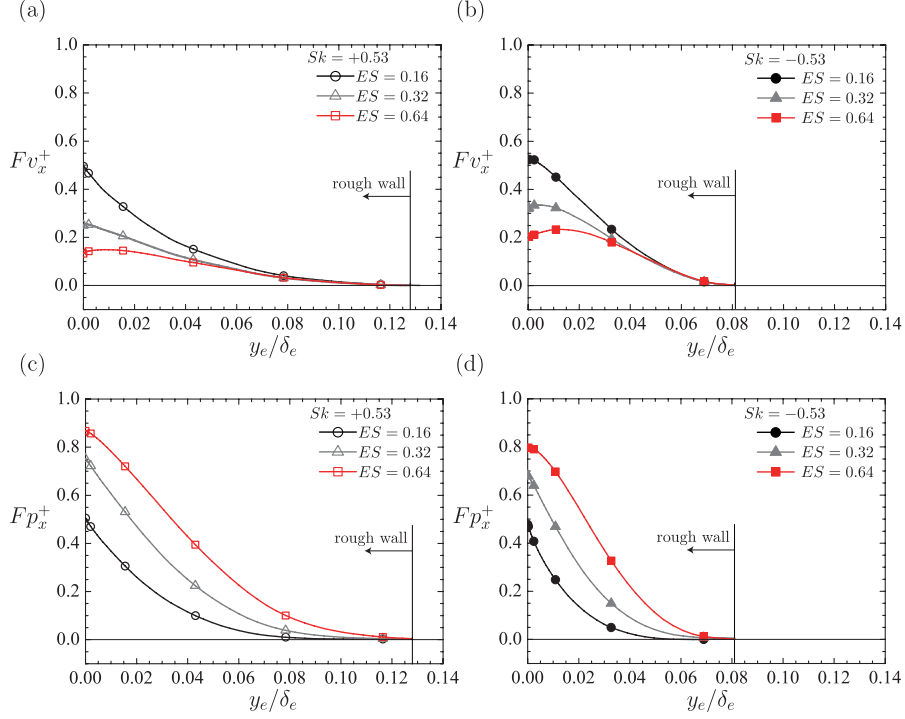


Figure 11: Drag force contribution in the double-averaged momentum equation: (a) viscous drag Fv_x^+ for cases with $Sk = +0.53$, (b) Fv_x^+ for cases with $Sk = -0.53$, (c) pressure drag Fp_x^+ for cases with $Sk = +0.53$, and (d) Fp_x^+ for cases with $Sk = -0.53$. The black thin line indicates the location of the maximum roughness crest.

siderably attenuated by the wall roughness. On the other hand, the increase in $\overline{s_w}^+$ away from the bottom is responsible for the increase in the surface area with the ES value. As a consequence of the change in the $\overline{s_w}^+$ profiles with ES , the contribution term H_w^+ increases with ES values, as shown in Fig.12(c,d).

As the wall interaction terms dominate the heat and momentum transfers below the maximum roughness crest, it is of importance to discuss the wall interaction terms to better understand the dissimilarity between heat and

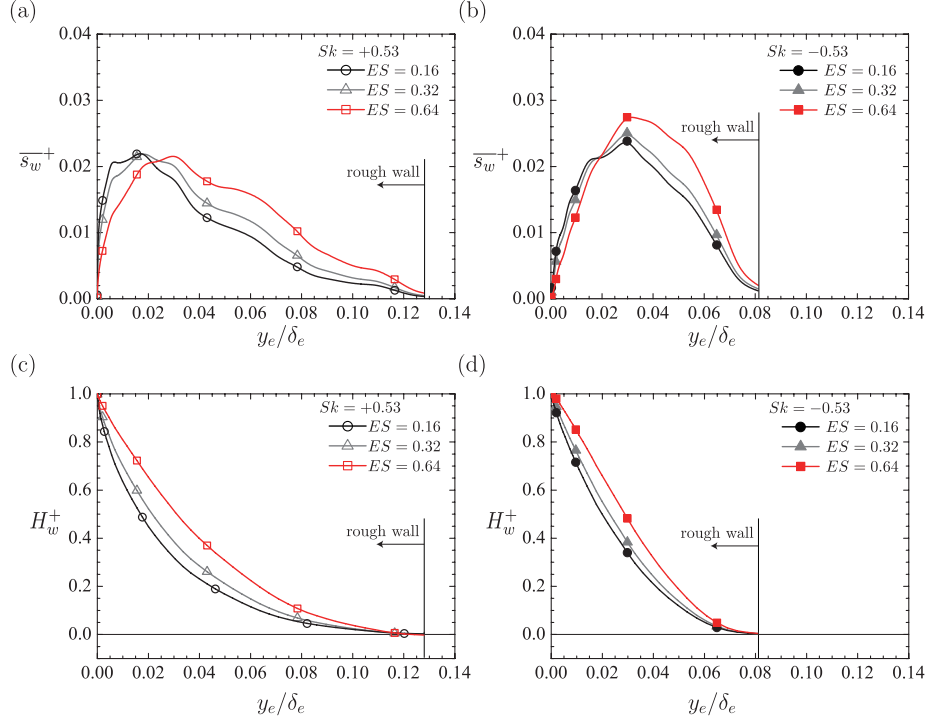


Figure 12: Wall heat transfer term s_w^+ and the corresponding contribution term H_w^+ : (a) $\overline{s_w}^+$ for cases with $Sk = +0.53$ and (b) $\overline{s_w}^+$ for cases with $Sk = -0.53$. (c) H_w^+ for the cases with $Sk = +0.53$ and (d) H_w^+ for cases with $Sk = -0.53$. The black thin line indicates the location of the maximum roughness crest.

momentum transfers. Figure 13 presents a comparison of the wall interaction terms, $\overline{f_{v_x}^+}$, $\overline{f_{p_x}^+}$, and $\overline{s_w}^+$ with the scaling of $y' = (y - h_m)/h_m$. The figure confirms that both $(\overline{f_{v_x}^+} + \overline{f_{p_x}^+})^+$ and $\overline{s_w}^+$ exhibit peak values just above the mean height of $0 < y' < 0.5$. A comparison of $(\overline{f_{v_x}^+} + \overline{f_{p_x}^+})^+$ and $\overline{s_w}^+$ confirms that, except for the case with $Sk = -0.53$ and $ES = 0.16$, the sum of the drag forces $(\overline{f_{v_x}^+} + \overline{f_{p_x}^+})^+$ is generally larger than $\overline{s_w}^+$ above the mean height of $y' > 0.2$, whereas $(\overline{f_{v_x}^+} + \overline{f_{p_x}^+})^+$ is smaller below the mean height of $y' < 0.1$. A possible explanation for $\overline{s_w}^+ > (\overline{f_{v_x}^+} + \overline{f_{p_x}^+})^+$ is a significant reduction in the

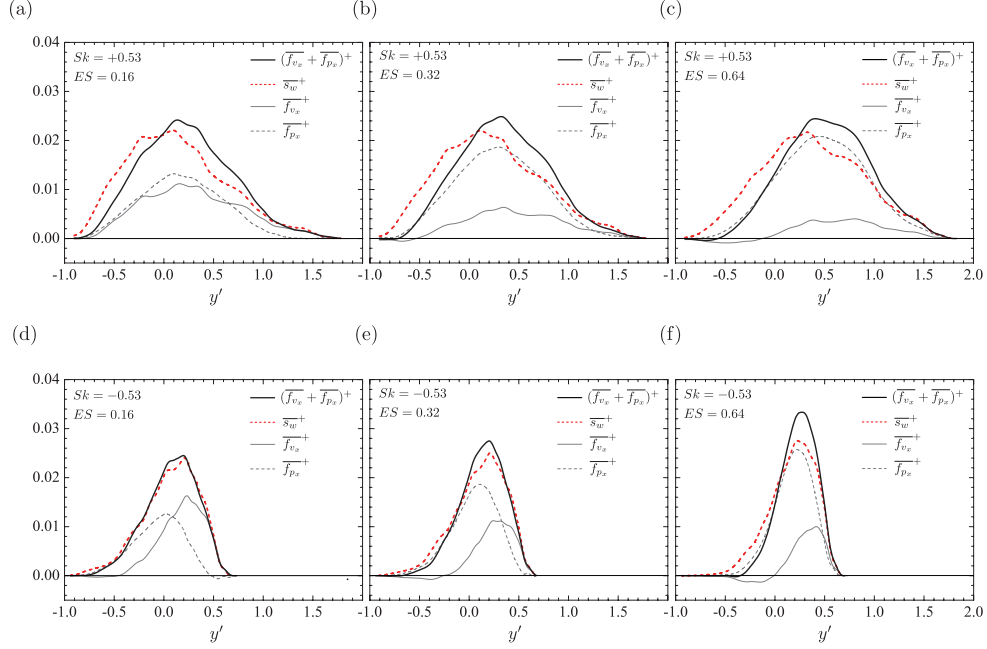


Figure 13: Comparison of the wall interaction terms with the scaling of $y' = (h - h_m)/h_m$: (a) for cases with $Sk = +0.53$ and $ES = 0.16$, (b) for cases with $Sk = +0.53$ and $ES = 0.32$, (c) for cases with $Sk = +0.53$ and $ES = 0.64$, (d) for cases with $Sk = -0.53$ and $ES = 0.16$, (e) for cases with $Sk = -0.53$ and $ES = 0.32$, and (f) for cases with $Sk = -0.53$ and $ES = 0.64$.

viscous drag $\overline{f_{v_x}^-}$ owing to the negative wall shear stress. The figure confirms that $\overline{f_{v_x}^+}$ decreases with the ES values, and it even takes a negative value below the mean roughness height ($y' < 0$). This trend is consistent with the observation from Kuwata and Nagura (2020), and is the result of the negative mean flow by a recirculating bubble behind the roughness crest as observed in the snapshots of the instantaneous velocity in Figure 14(a). On the other hand, for the temperature fields as shown in Fig.14(b), a thin thermal diffusive layer is formed in the vicinity of rough surfaces even in the

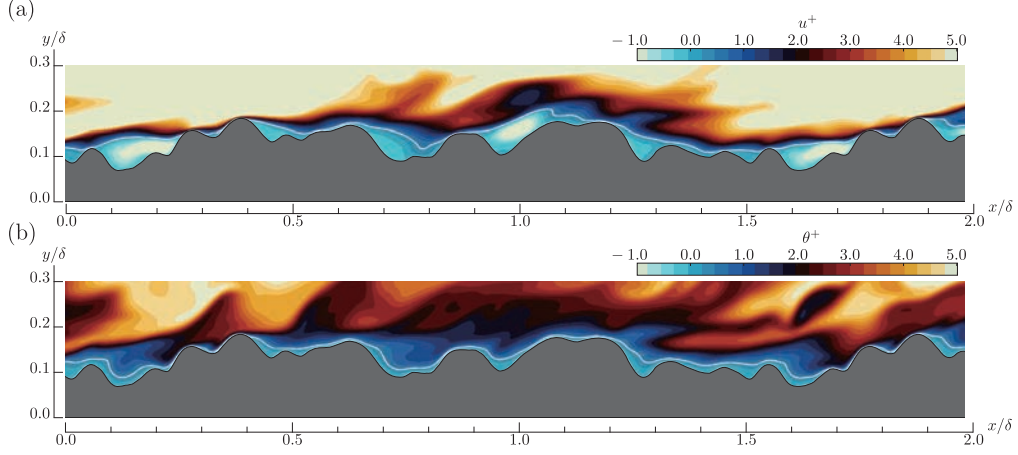


Figure 14: Snapshots of instantaneous u^+ and θ^+ in a $x-y$ plane at $z = 0$ for $Sk = -0.53$ and $ES = 0.64$; (a) u^+ , and (b) θ^+ . The white thin line indicates the iso-contour of $u^+ = 0.5$ and $\theta^+ = 0.5$.

recirculation region, as reported in MacDonald et al. (2019). It should be noted that, as the spatial variation of the local pressure induced by the wall roughness affects the flow fields, leading to the modification of $\overline{f_{v_x}^+}$. Hence, the pressure variation near the rough surface generates the pressure drag $\overline{f_{p_x}^+}$ but also has an indirect effect on the viscous drag $\overline{f_{v_x}^+}$ through the modification of the velocity fields. This indicates that the difference in the wall interaction terms for heat and momentum transfer cannot be directly attributed to $\overline{f_{p_x}^+}$. Indeed, for the case with $Sk = -0.53$ and $ES = 0.16$, as shown in Fig.13(d), although the pressure drag $\overline{f_{p_x}^+}$ occupies a large portion of $(\overline{f_{v_x}^+} + \overline{f_{p_x}^+})^+$, the profile of $\overline{s_w^+}$ collapses well onto $(\overline{f_{v_x}^+} + \overline{f_{p_x}^+})^+$.

3.3. Velocity and temperature roughness function

This subsection further discusses the momentum and energy budget terms to understand how they increase the roughness functions, as in (MacDonald et al., 2016; Jelly and Busse, 2018; Kuwata and Nagura, 2020). Although Kuwata and Nagura (2020) derived a mathematical expression for the contribution of momentum budgets to ΔU^+ , this subsection briefly summarizes the derivation and analysis result for the sake of completeness. In addition, we attempt to derive the contribution of energy budgets to $\Delta \Theta^+$. The mathematical expression of the contribution of the momentum budget to ΔU^+ starts from Eq.(28).

$$\frac{\partial \langle \bar{u} \rangle^+}{\partial y^+} = 1 - \frac{y_e}{\delta_e} + R_{12}^+ + \mathcal{T}_{12}^+ - Fv_x^+ - Fp_x^+, \quad (32)$$

The derivative of $\langle \bar{u} \rangle^+$ with respect to y^+ on the left-hand side of Eq.(32) can be transformed using the definition of y_e in Eq.(12) as follows:

$$\frac{\partial \langle \bar{u} \rangle^+}{\partial y^+} = \frac{\partial \varphi \langle \bar{u} \rangle^+}{\partial y_e^+} - \frac{\partial \varphi}{\partial y_e^+} \langle \bar{u} \rangle^+, \quad (33)$$

By integrating Eq.(32) using Eq.(33) over the wall-normal direction from 0 to y_e^+ , the mean velocity can be expressed in terms of the momentum budget terms as follows:

$$\begin{aligned} \varphi \langle \bar{u} \rangle^+(y_e^+) &= \frac{1}{Re_\tau} \left(Re_\tau y_e^+ - \frac{1}{2} (y_e^+)^2 \right) + \int_0^{y_e^+} (R_{12}^+ + \mathcal{T}_{12}^+) dy_e^+ \\ &\quad - \int_0^{y_e^+} Fv_x^+ dy_e^+ - \int_0^{y_e^+} Fp_x^+ dy_e^+ + \int_0^{y_e^+} \left(\frac{\partial \varphi}{\partial y_e^+} \langle \bar{u} \rangle^+ \right) dy_e^+, \end{aligned} \quad (34)$$

The roughness function ΔU^+ can be derived by subtracting Eq.(34) from the corresponding expression for a smooth wall at $y_e^+ = 100$. The resultant form

is expressed as follows:

$$\Delta U^+ = \Delta U_{td}^+ + \Delta U_{vd}^+ + \Delta U_{pd}^+ + \Delta U_{ir}^+, \quad (35)$$

where

$$\Delta U_{td}^+ = \int_0^{100} R_{12}^+ dy^+ \Big|_{smooth} - \int_0^{100} (R_{12}^+ + \mathcal{T}_{12}^+) dy_e^+, \quad (36)$$

$$\Delta U_{vd}^+ = \int_0^{h_{pe}^+} F v_x^+ dy_e^+, \quad (37)$$

$$\Delta U_{pd}^+ = \int_0^{h_{pe}^+} F p_x^+ dy_e^+, \quad (38)$$

$$\Delta U_{ir}^+ = - \int_0^{h_{pe}^+} \left(\frac{\partial \varphi}{\partial y_e^+} \langle \bar{u} \rangle^+ \right) dy_e^+, \quad (39)$$

where h_{pe} is the maximum roughness crest evaluated by y_e . Contributors ΔU_{td}^+ , ΔU_{vd}^+ , ΔU_{pd}^+ , and ΔU_{ir}^+ represent the effects of the sum of the plane-averaged Reynolds stress and plane-dispersive stress, viscous drag, pressure drag, and viscous terms related to the roughness density variation (Kuwata and Nagura, 2020). Note that $y_e^+ = y^+$ for the smooth wall because $\varphi = 1$. Furthermore, note that Eqs.(35)–(39) are not exactly the same as those in Kuwata and Nagura (2020) because Kuwata and Nagura (2020) further split the viscous drag term into the contributions of the plane-averaged velocity and its dispersion, as shown in Eq.(27).

The temperature roughness function can be derived by starting from Eq.(30):

$$\frac{1}{Pr} \frac{\partial \langle \bar{\theta} \rangle^+}{\partial y^+} = 1 - \frac{1}{\delta_e} \int_0^y \frac{\langle \bar{u} \rangle}{U_b} dy + H_2^+ + \mathcal{H}_2^+ - H_w^+. \quad (40)$$

In a similar fashion to the derivation of ΔU^+ , $\Delta \Theta^+$ can be decomposed into contribution terms as follows:

$$\Delta \Theta^+ = \Delta \Theta_{tot}^+ + \Delta \Theta_{td}^+ + \Delta \Theta_{fig12}^+ + \Delta \Theta_{ir}^+, \quad (41)$$

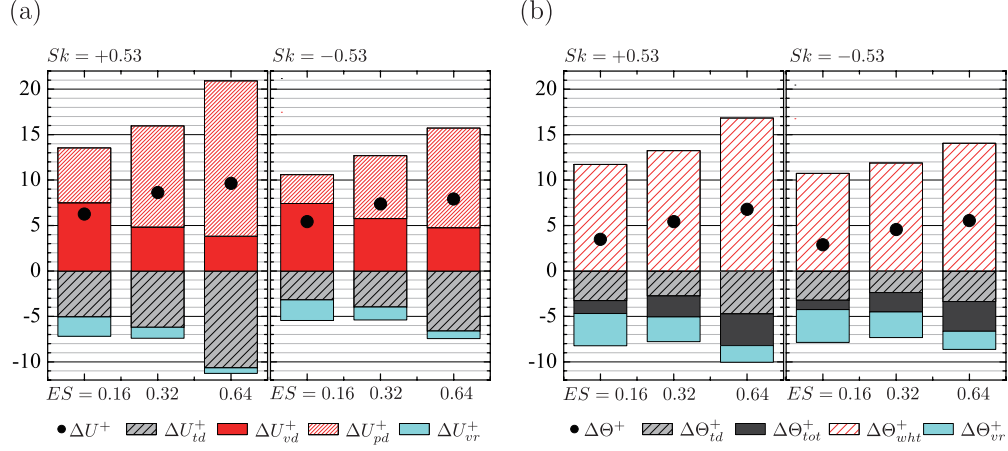


Figure 15: Contributors to the roughness functions: (a) contributors of Eqs.(37)–(39) to the velocity roughness function, and (b) contributors of Eqs.(43)–(45) to the temperature roughness function.

where

$$\Delta\Theta_{tot}^+ = \frac{Pr}{\delta_e} \int_0^{y_e^+} \left(\int_0^y \frac{\langle \bar{u} \rangle}{U_b} dy \right) dy_e^+ - \frac{Pr}{\delta} \int_0^{y^+} \left(\int_0^y \frac{\bar{u}}{U_b} dy \right) dy^+ \Big|_{smooth}, \quad (42)$$

$$\Delta\Theta_{td}^+ = Pr \int_0^{100} H_2^+ dy^+ \Big|_{smooth} - Pr \int_0^{100} (H_2^+ + \mathcal{H}_2^+) dy_e^+, \quad (43)$$

$$\Delta\Theta_{fig12}^+ = Pr \int_0^{h_{pe}^+} H_w^+ dy_e^+, \quad (44)$$

$$\Delta\Theta_{ir}^+ = -Pr \int_0^{h_{pe}^+} \left(\frac{\partial \varphi}{\partial y_e^+} \langle \bar{\theta} \rangle^+ \right) dy_e^+, \quad (45)$$

where the contributors $\Delta\Theta_{tot}^+$, $\Delta\Theta_{td}^+$, $\Delta\Theta_{fig12}^+$, and $\Delta\Theta_{ir}^+$ represent the effects of the total heat flux, the sum of the plane-averaged turbulent and plane-dispersion heat fluxes, wall heat transfer and conduction related to the roughness density variation, respectively.

The contributors to ΔU^+ in Eqs.(37)–(39) and $\Delta\Theta^+$ in Eqs.(43)–(45) are presented in Figure 15. What can be found immediately in Fig.15(a) is

that the increase in ΔU^+ is mainly attributed to the viscous and pressure drag contributions. As the ES value increases, the viscous drag contribution ΔU_{vd}^+ decreases, whereas the pressure drag contribution ΔU_{pd}^+ increases further, resulting in an increase in the drag force contribution $(\Delta U_{vd}^+ + \Delta U_{pd}^+)$. The negative contribution of ΔU_{td}^+ is due to the reduction in the sum of $-(R_{12}^+ + \mathcal{T}_{12}^+)$ by the wall roughness as shown in Fig.8, and this negative contribution partly cancels the increase in the positive contribution $(\Delta U_{vd}^+ + \Delta U_{pd}^+)$ with an increase in the ES value. Thus, the roughness function ΔU^+ does not substantially increase when the ES value increases from 0.32 to 0.64. This observation is consistent with those from Kuwata and Nagura (2020). Kuwata and Nagura (2020) may be referred to for the detailed physical explanations for this trend.

As for the temperature roughness function in Fig.15(b), the wall heat transfer $\Delta \Theta_{fig12}^+$ is the dominant mechanism for the increase in $\Delta \Theta^+$. Although $\Delta \Theta_{fig12}^+$ is generally smaller than the wall interaction term $(\Delta U_{vd}^+ + \Delta U_{pd}^+)$ for the velocity roughness function, $\Delta \Theta_{fig12}^+$ shows the same trend as $(\Delta U_{vd}^+ + \Delta U_{pd}^+)$. Another important observation in Fig.15(b) is that $\Delta \Theta_{td}^+$ and $\Delta \Theta_{tot}^+$ have a negative contribution to $\Delta \Theta^+$. The negative value of $\Delta \Theta_{tot}^+$ of Eq.(43) indicates that the total heat flux for the rough wall cases is lower than that for the smooth wall case, which is due to the reduction in the streamwise mean velocity by the wall roughness. On the other hand, the negative value of $\Delta \Theta_{td}^+$ is associated with a reduction in the sum of the turbulent and dispersion heat fluxes, $-(H_2^+ + \mathcal{H}_2^+)$, owing to the wall roughness, as observed in Fig.8. This is analogous to the corresponding term ΔU_{td}^+ for the velocity roughness function; however, the negative absolute value of $\Delta \Theta_{td}^+$

is smaller than that of ΔU_{id}^+ . This means that $-(R_{12}^+ + \mathcal{T}_{12}^+)$ is lower than $-(H_2^+ + \mathcal{H}_2^+)$. The primary reason for this is that the wall roughness decreases U^+ more than Θ^+ as shown in Fig.4. The reduction in U^+ more than Θ^+ results in a reduction in the mean velocity gradient to a greater extent than the temperature gradient near the rough surface. This leads to less generation of $-(R_{12}^+ + \mathcal{T}_{12}^+)$ than for $-(H_2^+ + \mathcal{H}_2^+)$ (Kuwata and Suga, 2016). The other possible reason is the role of the source term s_{cht} for constant heat flux conditions. Owing to the presence of s_{cht} in the energy equation, an additional term appears in the transport equation for the plane-averaged vertical turbulent heat flux H_2^+ , which is given as follows:

$$G_{2,\theta} = \langle \overline{s_{cht} \times v'} \rangle = \frac{A_r q_w}{\rho c Q L_x} R_{12}. \quad (46)$$

As $R_{12} < 0$ for the present flow system, $G_{2,\theta}$ acts as a production term for $-H_2^+$. Thus, the source term s_{cht} in the energy equation increases $-H_2^+$, which, in turn, results in a decrease in the negative contribution $\Delta \Theta_{id}^+$ through Eq.(44). The figure shows that the molecular viscous effects related to the roughness density variation (ΔU_{ir}^+ and $\Delta \Theta_{ir}^+$) exhibit negative contribution to ΔU^+ and $\Delta \Theta^+$, respectively. This is also evident from the definitions in Eqs.(39) and (45).

3.4. Dissimilarity between the heat and momentum transfer

Finally, the driving mechanisms of the dissimilarity between heat and momentum transfer are discussed. As indicated in Eq.(21), the Reynolds analogy factor RA for $Pr = 1$ can be expressed as a function of the skin friction coefficient and the difference between the velocity and temperature roughness functions ($\Delta U^+ - \Delta \Theta^+$). Hence, the Reynolds analogy holds when

$\Delta U^+ - \Delta \Theta^+ = 0$, whereas it breaks down on the negative side when $\Delta U^+ - \Delta \Theta^+ > 0$. To obtain a physical insight into the behavior of RA , we analyzed the growth of the mean velocity minus temperature $I^+ = \langle \bar{\theta} \rangle^+ - \langle \bar{u} \rangle^+$, which is referred to as the dissimilar indicator hereafter. Assuming that $Pr = 1$, we can derive I^+ using Eqs.(32) and (40) after some calculations, as follows:

$$\begin{aligned}
I^+ = & \underbrace{\frac{1}{\delta_e} \int_0^{y^+} \left(\int_0^y \frac{\varphi U_b - \langle \bar{u} \rangle}{U_b} dy \right) dy^+}_{I_{tot}^+} \\
& + \underbrace{\int_0^{y^+} \frac{\nu_{eff}}{Pr_{eff}} \left(Pr_{eff} \frac{\partial \langle \bar{u} \rangle^+}{\partial y^+} - \frac{\partial \langle \bar{\theta} \rangle^+}{\partial y^+} \right) dy^+}_{I_{td}^+} \\
& + \underbrace{\int_0^{y^+} \left[\int_{y^+}^{h_p^+} \left(\overline{f_{v_x}^+} + \overline{f_{p_x}^+} - \overline{s_w^+} \right) dy^+ \right] dy^+}_{I_{wi}^+}, \quad (47)
\end{aligned}$$

where I_{tot}^+ arises because of the difference between the total shear stress and heat flux profiles, I_{td}^+ represents the effects of turbulent and dispersion transports, and I_{wi}^+ represents the effects of the wall interaction.

Figure 16 shows a growth of these contribution terms with respect to y' . The dissimilar indicator I^+ shows an almost constant value of $I^+ \simeq 3$ in $y' > 0.5$ irrespective of the Sk and ES values, suggesting that I^+ for the present rough wall case is not significantly affected by the Sk and ES values. In addition, the figure shows that $\Delta U^+ - \Delta \Theta^+ \simeq I^+$ in $y' > 0.5$, which is due to the fact that the inner-scaled mean velocity and temperature profiles are nearly identical, $\overline{u}_{smooth}^+ \simeq \overline{\theta}_{smooth}^+$, when $Pr = 1$:

$$\Delta U^+ - \Delta \Theta^+ = \left(\overline{u}_{smooth}^+ - \langle \bar{u} \rangle^+ \right) - \left(\overline{\theta}_{smooth}^+ - \langle \bar{\theta} \rangle^+ \right) \simeq \langle \bar{\theta} \rangle^+ - \langle \bar{u} \rangle^+. \quad (48)$$

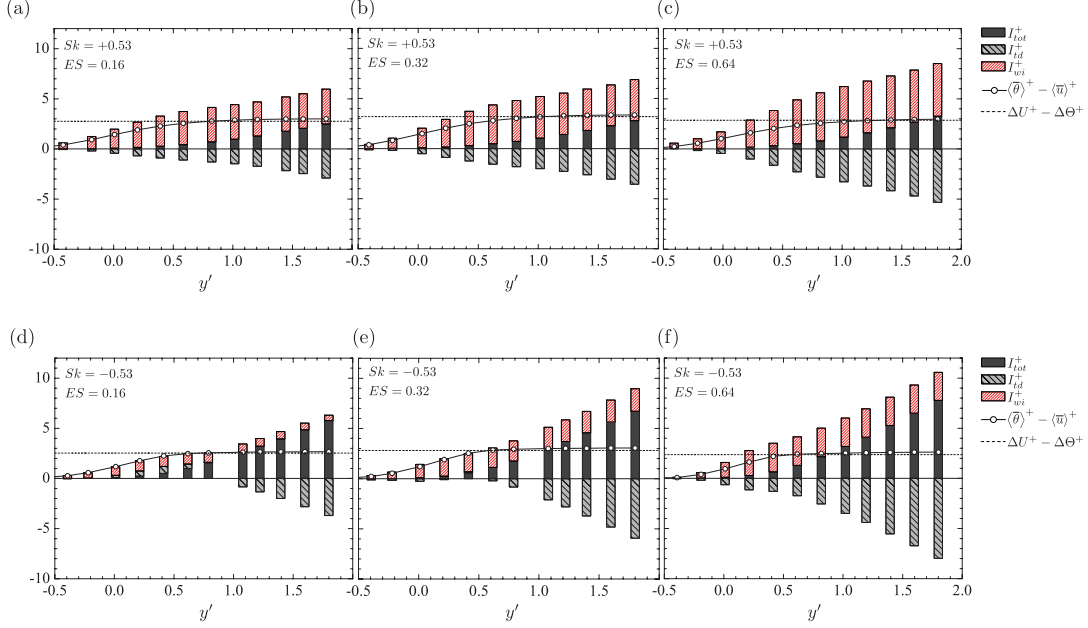


Figure 16: Growth of the contribution terms with respect to y' : (a) for cases with $Sk = +0.53$ and $ES = 0.16$, (b) for cases with $Sk = +0.53$ and $ES = 0.32$, (c) for cases with $Sk = +0.53$ and $ES = 0.64$, (d) for cases with $Sk = -0.53$ and $ES = 0.16$, (e) for cases with $Sk = -0.53$ and $ES = 0.32$, and (f) for cases with $Sk = -0.53$ and $ES = 0.64$.

This observation and the approximation of Eq.(21) indicate that the dependence of the topological parameters (Sk and ES) on the Reynolds analogy factor RA , as presented in Table 2, can be simply attributed to the dependence on C_f . Furthermore, as C_f can be expressed as a function of the equivalent sand-grain roughness k_s , RA for the present rough wall cases can be predicted solely by k_s . This may be the reason why the correlation in Eq(25) provides a reasonable prediction, as observed in Table 2.

When attention is given to the contribution of I^+ , it is found that in $y' > 0.5$, I_{tot}^+ consistently increases as it moves further away from the wall, whereas I_{td}^+ conversely decreases. As a result of these competing effects by I_{td}^+ and

I_{tot}^+ , I^+ in $y' > 0.5$ is almost unchanged, suggesting that the increase in I_{tot}^+ is canceled by I_{td}^+ . The other observation from Fig.16 is that, although the value of I^+ is unaffected by the Sk and ES values, the generation mechanisms for I^+ are quite different. Except for the case with $Sk = -0.53$ and $ES = 0.16$ in Fig.16(d), the dominant contributor to the increase in I^+ in $y' < 0.5$ is observed to be the positive value of the wall interaction I_{wi}^+ . The positive value of I_{wi}^+ indicates that the sum of the viscous and pressure drag forces exceeds the wall heat transfer term: (that is, $\overline{f_{vx}}^+ + \overline{f_{px}}^+ - \overline{s_w}^+ > 0$, as shown in Fig.13), whereas the negative value of I_{td}^+ is considered to be due to the reduction in the mean velocity gradient by the wall roughness from Eq.(47). In contrast, for the case with $Sk = -0.53$ and $ES = 0.16$, as shown in Fig.16(d), the term related to the turbulent and dispersion transport I_{td}^+ in $y' < 0.5$ acts as a positive contribution for I^+ and I_{wi}^+ . The positive value for I_{td}^+ is considered to be due to two combined factors: One is the relatively moderate reduction in the mean velocity gradient near the rough wall in comparison with the other cases, and the other is the rapid increase in the effective Prandtl number Pr_{eff} toward the bottom, as shown in Fig.9 (a). Thus, the integrand $Pr_{eff}\partial\langle\bar{u}\rangle^+/\partial y^+ - \partial\langle\bar{\theta}\rangle^+/\partial y^+$ for I_{td}^+ in Eq.(47) is positive, resulting in the positive value of I_{td}^+ . Note that the region of the abrupt increase and decrease in Pr_{eff} ($y_e/\delta_e < 0.01$) as shown in Fig.9 roughly corresponds to the region of $y' < 0$ where the contribution of I_{td}^+ is considerably smaller than I_{wi}^+ . Hence, the abrupt increase and decrease in Pr_{eff} may not have a significant impact on the dissimilarity between heat and momentum transfer. To get more insight into the mechanisms of the dissimilarity, it would be better to analyze the simulations with uniform

heat generation at $Pr = 1.0$ in which the energy equation completely similar to the streamwise momentum equation (Kasagi et al., 2010).

Conclusion

This study examines the effects of rough surface topography on heat and momentum transfer through DNSs on turbulent heat transfer over uniformly heated three-dimensional irregular rough surfaces where the effective slope ES and skewness Sk values are systematically varied while maintaining a fixed root-mean-square roughness. The DNSs were conducted at a friction Reynolds number of 450 in open-channel flows through the double-distribution-function LBM, in which the time evolutions of the particle and energy density distribution functions are solved. The temperature is treated as a passive scalar with a Prandtl number of unity, neglecting buoyancy effects.

The augmentation of the skin friction coefficient and Stanton number by the wall roughness are observed to be larger for positively skewed surfaces with larger effective slope values. However, the Reynolds analogy factor RA , which is the ratio of the doubled Stanton number to the skin friction coefficient, is smaller than the corresponding value for a smooth wall turbulence, and tends to decrease with an increase in the skin friction coefficient. This trend is reasonably predicted solely by the inner-scaled equivalent sand-grain roughness, suggesting that the relationship between the Reynolds analogy factor and the equivalent sand-grain roughness is not affected by the effective slope and skewness values.

Analysis of the heat and momentum transfer mechanisms based on the spatial- and time-averaged equations suggests that the reduction in RA due to the wall roughness can be attributed to two factors. The first factor is a rapid increase in the effective Prandtl number within the rough wall: the

effective thermal diffusivity due to the combined effects of turbulence and dispersion is much smaller than the effective momentum diffusivity within the rough wall. This is found to be one of the reasons for the reduction in RA for a negatively skewed surface with a smaller effective slope. As for the second factor, the dominant mechanism for the reduction in RA is found to be an increase in the drag force term relative to the wall heat transfer term. Below the mean surface height, the sum of the viscous and pressure drag terms is smaller than the wall heat transfer term, which acts as an increase in RA . Conversely, above the mean surface height, the sum of the pressure and viscous drag terms considerably overwhelms the wall heat transfer. Consequently, the contribution of the drag force term to the momentum transfer is more significant than that of the wall heat transfer to the heat transfer, resulting in the reduction in RA .

The present DNS study can provide information on the mechanisms of dissimilarity between heat and momentum transfers, which would be useful for predicting and controlling the heat transfer augmentation due to the wall roughness. However, owing to limitations in computational resources, the present study only considers flows with a single Prandtl number at a single Reynolds number. Further analysis of the effects of the Prandtl number and Reynolds number is essential for the optimal design of wall roughness to enhance heat transfer.

Finally, it should be noted that the above conclusion is drawn based on DNSs under constant heat flux conditions. However, we have also performed preliminary DNSs with the uniform heat generation and confirmed that the conclusion is unaffected by the choice of the thermal boundary conditions.

Appendix A: Modified mixed boundary condition for rough surface

A widely used approach for the uniform heat flux condition for the DNS is the so-called mixed boundary condition proposed by Kasagi et al. (1992). This mixed boundary condition imposes a constant wall temperature with a source term such that the local mean temperature increases linearly in the streamwise direction. This approach may be directly applied for a rough surface as in Forooghi et al. (2018a), who prescribe a constant streamwise temperature gradient, neglecting the spatial variation in the rough surface area. However, the streamwise temperature gradient depends on the surface area of the rough surface area. Therefore, in this study, to account for the influence of spatial variation in the rough surface area, we extend the mixed boundary condition for a rough surface. Under uniform heat flux conditions, the time-averaged energy budget can be expressed as follows:

$$\rho c \int_0^{L_y} \int_0^{L_z} \overline{uT}(x+dx, y, z) dydz - \rho c \int_0^{L_y} \int_0^{L_z} \overline{uT}(x, y, z) dydz = q_w dA_r, \quad (\text{A1})$$

where dA_r is the infinitesimal surface area in the region $[x, x+dx] \times [0, L_y] \times [0, L_z]$, which is approximated by the length scale of $\ell_{yz}(x)$ as $dA_r = \ell_{yz}(x) dx$ in this study. By dividing the flow rate Q , defined as $Q = \int_0^{L_y} \int_0^{L_z} \overline{u} dydz$, we can rewrite the energy budget in terms of the bulk temperature T_b as follows:

$$\rho c T_b(x+dx) - \rho c T_b(x) = \frac{q_w}{Q} dx \ell_{yz}(x). \quad (\text{A2})$$

Hence, the streamwise bulk mean temperature gradient can be expressed as follows:

$$\frac{\partial T_b}{\partial x} = \frac{q_w}{\rho c Q} \ell_{yz}(x). \quad (\text{A3})$$

The local fluid temperature T can be decomposed into the wall temperature T_w and temperature variance Θ as follows:

$$T(x, y, z, t) = T_w(x) - \theta(x, y, z, t), \quad (\text{A4})$$

where the wall temperature is $T_w(x) = T_{w0} + \int_0^x \frac{dT_b}{dx} dx$, where T_{w0} is the wall temperature at $x = 0$. Substituting the definition of temperature variance in Eq.A4 into the energy equation for an incompressible fluid, we can derive the energy equation in terms of θ as follows:

$$\frac{\partial \theta}{\partial t} + u_j \frac{\partial \theta}{\partial x_j} = \alpha \frac{\partial^2 \theta}{\partial x_j^2} - \underbrace{\frac{q_w}{\rho c Q} \left(\alpha \frac{d\ell_{yz}(x)}{dx} - u\ell_{yz}(x) \right)}_{s_{cht}}. \quad (\text{A5})$$

where $x_1 = x$, $x_2 = y$, and $x_3 = z$. For the present DNSs with the modified mixed boundary condition, a transformed temperature $\theta = T - T_w$ is obtained by solving Eq.(A5), assuming that the wall temperature is zero. Note that the expression of s_{cht} is reduced to that of the smooth wall when $\ell_{yz}(x) = L_z$.

Appendix B: Heat flux balance in the double-averaged system

Applying integration to the double-averaged energy equation over the wall-normal direction from 0 to y , the integrated energy equation for the present flow system can be expressed as

$$0 = \alpha \frac{\partial \langle \bar{\theta} \rangle}{\partial y} - H_2 - \mathcal{H}_2 - \int_0^y \bar{s}_w dy + \int_0^y \langle \bar{s}_{cht} \rangle dy + C, \quad (\text{B1})$$

where C is an integration constant, and it can be determined such that the total heat flux at the top adiabatic wall is zero, expressed as follows:

$$C = \int_0^\delta \bar{s}_w dy - \int_0^\delta \langle \bar{s}_{cht} \rangle dy, \quad (\text{B2})$$

As $\overline{s_w}$ only has a nonzero value below the maximum roughness crest ($y < h_p$), the interval of integration for $\overline{s_w}$ can be rewritten as

$$C = \int_0^{h_p} \overline{s_w} dy - \int_0^\delta \langle \overline{s_{cht}} \rangle dy. \quad (\text{B3})$$

Substituting Eq.(B1) into Eq.(B3), we can rewrite the integrated energy equation as follows:

$$0 = \alpha \frac{\partial \langle \overline{\theta} \rangle}{\partial y} - H_2 - \mathcal{H}_2 + \underbrace{\left(\int_0^\delta \overline{s_w} dy - \int_0^y \overline{s_w} dy \right)}_{H_{fig12}} - \underbrace{\left(\int_0^\delta \langle \overline{s_{cht}} \rangle dy - \int_0^y \langle \overline{s_{cht}} \rangle dy \right)}_{S_{cht}}. \quad (\text{B4})$$

The interval of integration for the wall heat transfer term H_{fig12} can be rewritten as

$$H_{fig12} = \int_0^\delta \overline{s_w} dy - \int_0^y \overline{s_w} dy = \int_y^\delta \overline{s_w} dy. \quad (\text{B5})$$

From the definition of the plane averaging in Eq.(8), the plane-averaged source term in the source term contribution S_{cht} is expressed as follows:

$$\begin{aligned} \langle \overline{s_{cht}} \rangle &= -\frac{1}{A} \int_0^{L_z} \int_0^{L_x} \frac{q_w}{\rho c Q} \left(\alpha \frac{d\ell_{yz}(x)}{dx} - u\ell_{yz}(x) \right) dx dz \\ &= -\frac{q_w \alpha}{A \rho c Q} \int_0^{L_x} \frac{d\ell_{yz}(x)}{dx} dx \int_0^{L_z} dz + \frac{q_w}{A \rho c Q} \int_0^{L_z} \int_0^{L_x} u\ell_{yz}(x) dx dz, \end{aligned} \quad (\text{B6})$$

The first term on the right-hand side of Eq.(B6) is zero because of the periodicity $\ell_{yz}(0) = \ell_{yz}(L_x)$. Considering a sufficiently large rough surface with a homogeneous and isotropic nature, $\ell_{yz}(x)$ is no longer a function of x , but can be approximated as a constant value A_r/L_x . Hence, Eq.(B6) can be

simplified as follows:

$$\langle \overline{s_{cht}} \rangle \simeq \frac{q_w A_r}{\rho c Q L_x} \langle \overline{u} \rangle. \quad (\text{B7})$$

The flow rate Q can be expressed as a product of the bulk mean velocity U_b and the effective $y - z$ plane area $\delta_e L_z$ (Kuwata and Kawaguchi, 2019). The source term S_{cht} can be expressed using Eq.(B7) as follows:

$$\begin{aligned} S_{cht} &= \frac{q_{wa}}{\rho c \delta_e U_b} \int_0^\delta \langle \overline{u} \rangle dy - \frac{q_{wa}}{\rho c \delta_e U_b} \int_0^y \langle \overline{u} \rangle dy \\ &= \frac{q_{wa}}{\rho c} - \frac{q_{wa}}{\rho c} \frac{1}{\delta_e} \int_0^y \frac{\langle \overline{u} \rangle}{U_b} dy, \end{aligned} \quad (\text{B8})$$

Here, the definition of the equivalent heat flux $q_{wa} = q_w A_r / A$ is used. Therefore, the total heat flux budget normalized by $u_\tau t_\tau = q_{wa} / (\rho c)$ can be expressed as follows:

$$1 - \frac{1}{\delta_e} \int_0^y \frac{\langle \overline{u} \rangle}{U_b} dy = \frac{1}{Pr} \frac{\partial \langle \overline{\theta} \rangle^+}{\partial y^+} - H_2^+ - \mathcal{H}_2^+ + \underbrace{\int_{y^+}^{h_p^+} s_w^+ dy^+}_{H_{fig12}^+}. \quad (\text{B9})$$

Acknowledgements

The author expresses the gratitude to their colleagues, Ph.D. K. Suga and Dr. M. Kaneda, for their support. This study was partly financially supported by a research grant (No.17K14591) from JSPS Japan. Numerical calculations were performed on a TSUBAME3.0 supercomputer at the Tokyo Institute of Technology (ID: hp190065).

References

Abe, H., Kawamura, H., Matsuo, Y., 2004. Surface heat-flux fluctuations in a turbulent channel flow up to $Re_\tau = 1020$ with $Pr = 0.025$ and 0.71 . *Int. J. Heat Fluid Flow* 25, 404–419.

- Acharya, M., Bornstein, J., Escudier, M., 1986. Turbulent boundary layers on rough surfaces. *Exp. Fluids* 4, 33–47.
- Akermann, K., Renze, P., Dietl, J., Schröder, W., 2020. Large-eddy simulation of turbulent heat transfer in a multiple-started helically rib-roughened pipe. *Int. J. Heat Mass Transfer* 154, 119667.
- Bons, J., Taylor, R., McClain, S., Rivir, R., 2001. The many faces of turbine surface roughness. *J. Turbomach.* 123, 739–748.
- Bons, J.P., 2002. St and cf augmentation for real turbine roughness with elevated freestream turbulence, in: *ASME Turbo Expo 2002: Power for Land, Sea, and Air*, American Society of Mechanical Engineers. pp. 349–363.
- Bragg, M., Gregorek, G., Lee, J., 1986. Airfoil aerodynamics in icing conditions. *J. Aircraft* 23, 76–81.
- Chamoli, S., Thakur, N., Saini, J., 2012. A review of turbulence promoters used in solar thermal systems. *Renew. Sust. Energ. Rev.* 16, 3154–3175.
- Chan, L., MacDonald, M., Chung, D., Hutchins, N., Ooi, A., 2015. A systematic investigation of roughness height and wavelength in turbulent pipe flow in the transitionally rough regime. *J. Fluid Mech.* 771, 743–777.
- Clauser, F., 1954. Turbulent boundary layers in adverse pressure gradients. *J. Aeronautical Sciences* 21, 91–108.
- Coceal, O., Thomas, T., Castro, I., Belcher, S., 2006. Mean flow and tur-

- bulence statistics over groups of urban-like cubical obstacles. *Boundary Layer Meteorol.* 121, 491–519.
- Crimaldi, J., Koseff, J., Monismith, S., 2006. A mixing-length formulation for the turbulent Prandtl number in wall-bounded flows with bed roughness and elevated scalar sources. *Phys. Fluids* 18, 095102.
- De Marchis, M., 2016. Large eddy simulations of roughened channel flows: Estimation of the energy losses using the slope of the roughness. *Comput. Fluids* 140, 148–157.
- De Marchis, M., Napoli, E., Armenio, V., 2010. Turbulence structures over irregular rough surfaces. *J. Turb.* 11, 1–32.
- Dipprey, D., Sabersky, R., 1963. Heat and momentum transfer in smooth and rough tubes at various prandtl numbers. *Int. J. Heat Mass Transfer* 6, 329–353.
- Dirling, JR, R., 1973. A method for computing rough wall heat transfer rates on reentry nosetips, in: 8th Thermophysics Conference, p. 763.
- Dvorak, F., 1969. Calculation of turbulent boundary layers on rough surfaces in pressure gradient. *AIAA journal* 7, 1752–1759.
- Dwyer, M., Patton, E., Shaw, R., 1997. Turbulent kinetic energy budgets from a large-eddy simulation of airflow above and within a forest canopy. *Boundary-Layer Meteorol.* 84, 23–43.
- Flack, K., Schultz, M., Barros, J., 2020. Skin friction measurements of

- systematically-varied roughness: Probing the role of roughness amplitude and skewness. *Flow, Turb. Combust.* 104, 317–329.
- Flack, K., Schultz, M., Connelly, J., 2007. Examination of a critical roughness height for outer layer similarity. *Phys. Fluids* 19, 095104.
- Flack, K.A., Schultz, M.P., 2010. Review of hydraulic roughness scales in the fully rough regime. *J. Fluids Engng.* 132, 041203.
- Flack, K.A., Schultz, M.P., 2014. Roughness effects on wall-bounded turbulent flows. *Phys. Fluids* 26, 101305.
- Flack, K.A., Schultz, M.P., Barros, J.M., Kim, Y.C., 2016. Skin-friction behavior in the transitionally-rough regime. *Int. J. Heat Fluid Flow* 61, 21–30.
- Forooghi, P., Stripf, M., Frohnafel, B., 2018a. A systematic study of turbulent heat transfer over rough walls. *Int.l J. Heat Mass Transfer* 127, 1157–1168.
- Forooghi, P., Stroh, A., Magagnato, F., Jakirlić, S., Frohnafel, B., 2017. Toward a universal roughness correlation. *J. Fluids Engng.* 139, 121201.
- Forooghi, P., Stroh, A., Schlatter, P., Frohnafel, B., 2018b. Direct numerical simulation of flow over dissimilar, randomly distributed roughness elements: A systematic study on the effect of surface morphology on turbulence. *Phys. Rev. Fluids* 3, 044605.
- Gee, D., Webb, R., 1980. Forced convection heat transfer in helically rib-roughened tubes. *Int. J. Heat Mass Transfer* 23, 1127–1136.

- Gowen, R., Smith, J., 1968. Turbulent heat transfer from smooth and rough surfaces. *Int. J. Heat Mass Transfer* 11, 1657–1674.
- Hama, F.R., 1954. Boundary layer characteristics for smooth and rough surfaces. *Trans. Soc. Nav. Arch. Marine Engrs.* 62, 333–358.
- Hasegawa, Y., Kasagi, N., 2011. Dissimilar control of momentum and heat transfer in a fully developed turbulent channel flow. *J. Fluid Mech.* 683, 57–93.
- Ikeda, T., Durbin, P., 2007. Direct simulations of a rough-wall channel flow. *J. Fluid Mech.* 571, 235–263.
- Jelly, T., Busse, A., 2018. Reynolds and dispersive shear stress contributions above highly skewed roughness. *J. Fluid Mech.* 852, 710–724.
- Jelly, T., Busse, A., 2019. Reynolds number dependence of Reynolds and dispersive stresses in turbulent channel flow past irregular near-gaussian roughness. *Int. J. Heat Fluid Flow* 80, 108485.
- Jiménez, J., 2004. Turbulent flows over rough walls. *Annu. Rev. Fluid Mech.* 36, 173–196.
- Kader, B., 1981. Temperature and concentration profiles in fully turbulent boundary layers. *Int. J. Heat Mass Transfer* 24, 1541–1544.
- Kaithakkal, A., Kametani, Y., Hasegawa, Y., 2020. Dissimilarity between turbulent heat and momentum transfer induced by a streamwise travelling wave of wall blowing and suction. *J. Fluid Mech.* 886.

- Kasagi, N., Hasegawa, Y., Fukagata, K., Iwamoto, K., 2010. Control of turbulent transport: Less friction and more heat transfer, in: Int. Heat Transfer Conf., pp. 309–324.
- Kasagi, N., Tomita, Y., Kuroda, A., 1992. Direct numerical simulation of passive scalar field in a turbulent channel flow. *Journal of Heat Transfer* 114, 598–606.
- Kato, K., Choi, K.S., Azuma, T., 2000. Heat-transfer enhancement and pressure loss by surface roughness in turbulent channel flows. *Int. J. Heat Mass Transfer* 43, 4009–4017.
- Kawamura, H., Ohsaka, K., Abe, H., Yamamoto, K., 1998. DNS of turbulent heat transfer in channel flow with low to medium-high Prandtl number fluid. *Int. J. Heat Fluid Flow* 19, 482–491.
- Kays, W.M., Crawford, M., 1993. *Convective Heat and Mass Transfer*, 3rd Edition. McGraw-Hill, New York, NY.
- Kozuka, M., Seki, Y., Kawamura, H., 2009. DNS of turbulent heat transfer in a channel flow with a high spatial resolution. *Int. J. Heat Fluid Flow* 30, 514–524.
- Kuwahara, F., Nakayama, A., Koyama, H., 1996. A Numerical Study of Thermal Dispersion in Porous Media. *J. Heat Transfer* 118, 756–761.
- Kuwata, Y., Kawaguchi, Y., 2018. Statistical discussions on skin frictional drag of turbulence over randomly distributed semi-spheres. *Int. J. Adv. Engng. Sci. Appl. Mat.* , 1–10.

- Kuwata, Y., Kawaguchi, Y., 2019. Direct numerical simulation of turbulence over systematically varied irregular rough surfaces. *J. Fluid Mech.* 862, 781–815.
- Kuwata, Y., Nagura, R., 2020. Direct numerical simulation on the effects of surface slope and skewness on rough-wall turbulence. *Phys. Fluids* 32, 105113.
- Kuwata, Y., Suga, K., 2016. Transport mechanism of interface turbulence over porous and rough walls. *Flow, Turb. Combust.* 97, 1071–1093.
- Kuwata, Y., Sugiyama, T., Kawaguchi, Y., 2020. On the scaling of turbulence over an irregular rough surface in a transitionally rough regime. *J. Therm.l Sci. Tech.* 15, 0015.
- Latt, J., Chopard, B., 2006. Lattice Boltzmann method with regularized pre-collision distribution functions. *Math. Comput. Simulat.* 72, 165–168.
- Leonardi, S., Castro, I., 2010. Channel flow over large cube roughness: a direct numerical simulation study. *J. Fluid Mech.* 651, 519–539.
- Li, L., Mei, R., Klausner, J., 2014. Heat transfer evaluation on curved boundaries in thermal lattice boltzmann equation method. *J. heat transfer* 136.
- Lluesma-Rodríguez, F., Hoyas, S., Perez-Quiles, M.J., 2018. Influence of the computational domain on dns of turbulent heat transfer up to $re\tau = 2000$ for $pr = 0.71$. *Int. J. Heat Mass Transfer* 122, 983–992.
- Lynch, F., Khodadoust, A., 2001. Effects of ice accretions on aircraft aerodynamics. *Progress in Aerospace Sciences* 37, 669–767.

- MacDonald, M., Chan, L., Chung, D., Hutchins, N., Ooi, A., 2016. Turbulent flow over transitionally rough surfaces with varying roughness densities. *J. Fluid Mech.* 804, 130–161.
- MacDonald, M., Hutchins, N., Chung, D., 2019. Roughness effects in turbulent forced convection. *J. Fluid Mechanics* 861, 138–162.
- Martinelli, R., 1947. Heat transfer to molten metals. *Trans. Am. Soc. Mech. Eng.* 69, 947–959.
- Miyake, Y., Tsujimoto, K., Nakaji, M., 2001. Direct numerical simulation of rough-wall heat transfer in a turbulent channel flow. *Int. J. Heat Fluid Flow* 22, 237–244.
- Mochizuki, S., Murata, A., Shibata, R., Yang, W.J., 1999. Detailed measurements of local heat transfer coefficients in turbulent flow through smooth and rib-roughened serpentine passages with a 180 sharp bend. *Int. J. Heat Mass Transfer* 42, 1925–1934.
- Murata, A., Mochizuki, S., 2001. Comparison between laminar and turbulent heat transfer in a stationary square duct with transverse or angled rib turbulators. *Int. J. Heat Mass Transfer* 44, 1127–1141.
- Musker, A., 1980. Universal roughness functions for naturally-occurring surfaces. *Trans. Canadian Soc. Mech. Engng.* 6, 1–6.
- Nagano, Y., Hattori, H., Houra, T., 2004. DNS of velocity and thermal fields in turbulent channel flow with transverse-rib roughness. *Int. J. Heat Fluid Flow* 25, 393–403.

- Napoli, E., Armenio, V., De Marchis, M., 2008. The effect of the slope of irregularly distributed roughness elements on turbulent wall-bounded flows. *J. Fluid Mech.* 613, 385–394.
- Nikuradse, J., 1933. Laws of flow in rough pipes, in: *VDI Forschungsheft*, Citeseer.
- Nishiyama, Y., Kuwata, Y., Suga, K., 2020. Direct numerical simulation of turbulent heat transfer over fully resolved anisotropic porous structures. *Int. J. Heat Fluid Flow* 81, 108515.
- Nunner, W., 1956. Heat transfer and pressure drop in rough tubes, in: *VDI Forschungsheft*, pp. 5–39.
- Pan, C., Luo, L.S., Miller, C., 2006. An evaluation of lattice boltzmann schemes for porous medium flow simulation. *Comput. Fluids* 35, 898–909.
- Peeters, J., Sandham, N., 2019. Turbulent heat transfer in channels with irregular roughness. *Int. J. Heat Mass Transfer* 138, 454–467.
- Schlichting, H., 1937. Experimental investigation of the problem of surface roughness. 823, National Advisory Committee for Aeronautics.
- Schultz, M., 2007. Effects of coating roughness and biofouling on ship resistance and powering. *Biofouling* 23, 331–341.
- Schultz, M., Flack, K., 2005. Outer layer similarity in fully rough turbulent boundary layers. *Exp. Fluids* 38, 328–340.
- Schultz, M.P., Flack, K.A., 2009. Turbulent boundary layers on a systematically varied rough wall. *Phys. Fluids* 21, 015104.

- Sigal, A., Danberg, J., 1990. New correlation of roughness density effect on the turbulent boundary layer. *AIAA journal* 28, 554–556.
- Spalart, P., Strelets, M., 2000. Mechanisms of transition and heat transfer in a separation bubble. *J. Fluid Mech.* 403, 329–349.
- Suga, K., Chikasue, R., Kuwata, Y., 2017. Modelling turbulent and dispersion heat fluxes in turbulent porous medium flows using the resolved les data. *Int. J. Heat Fluid Flow* 68, 225–236.
- Suga, K., Kuwata, Y., Takashima, K., Chikasue, R., 2015. A D3Q27 multiple-relaxation-time lattice Boltzmann method for turbulent flows. *Comput. Math. Appl.* 69, 518–529.
- Thakkar, M., Busse, A., Sandham, N.D., 2017. Surface correlations of hydrodynamic drag for transitionally rough engineering surfaces. *J. Turb.* 18, 138–169.
- Townsin, R., Byrne, D., Svensen, T., Milne, A., 1981. Estimating the technical and economic penalties of hull and propeller roughness. *Trans. SNAME* 89, 295–318.
- Van Rij, J.A., Belnap, B., Ligrani, P., 2002. Analysis and experiments on three-dimensional, irregular surface roughness. *ASME, Transactions, J. Fluids Engng.* 124, 671–677.
- Wassel, A., Mills, A., 1979. Calculation of variable property turbulent friction and heat transfer in rough pipes. *J. Heat Transfer* 101, 469–474.

- Webb, R., Eckert, E., Goldstein, R., 1971. Heat transfer and friction in tubes with repeated-rib roughness. *Int. J. Heat Mass Transfer* 14, 601–617.
- Yaglom, A., Kader, B., 1974. Heat and mass transfer between a rough wall and turbulent fluid flow at high Reynolds and Peclet numbers. *J. Fluid Mech.* 62, 601–623.
- Yamamoto, A., Hasegawa, Y., Kasagi, N., 2013. Optimal control of dissimilar heat and momentum transfer in a fully developed turbulent channel flow. *J. Fluid Mech.* 733, 189.
- Yuan, J., Piomelli, U., 2014. Roughness effects on the reynolds stress budgets in near-wall turbulence. *J. Fluid Mech.* 760.
- Zerda, T., Yuan, X., Moore, S., y Leon C.A., L., 1999. Surface area, pore size distribution and microstructure of combustion engine deposits. *Carbon* 37.